https://doi.org/10.5194/egusphere-2026-62
Preprint. Discussion started: 22 January 2026

Seasonal and Inter-Annual Evolution of the Deformation of Two Arctic Landslides

Andreas Aspaas[1,2], Grégory Bievre[3], Pascal Lacroix[3], Nadège Langet[4], Juditha Aga[5], Ingrid Skrede[2], Lene Kristensen[2], Bernd Etzelmüller[5], and François Renard[1,3]

[1]The Njord Centre, Departments of Geosciences and Physics, University of Oslo, Oslo, Norway
[2]Section for Landslides and Avalanches, Norwegian Water Resources and Energy Directorate, Norway
[3]Univ. Grenoble Alpes, Grenoble INP, Univ. Savoie Mont Blanc, CNRS, IRD, Univ. Gustave Eiffel, ISTerre, Grenoble, France
[4]Department of Applied Seismology, NORSAR, Kjeller, Norway
[5]Department of Geosciences, University of Oslo, 0313 Oslo, Norway

Correspondence: Andreas Aspaas (agas@nve.no)

Abstract. Landslides in glacial and periglacial environments are increasingly affected by climate change, with rapid failures reported in high mountain regions and the Arctic. The complex mechanisms behind these events are often poorly understood due to a lack of dense in situ data. We investigate two slow-moving landslides in Arctic Norway (70° N), the Jettan and Gámanjunni landslides, located about 10 km apart, with Jettan below and Gámanjunni above the permafrost boundary. Using over a decade of multi-physics observations, including geodetic, borehole, seismic, and hydrological data, we examine surface and subsurface deformation. Both landslides display similar seasonal surface velocity patterns, with peaks in spring and autumn, likely influenced by pore-water infiltration. At Jettan, twelve years of inclinometer data in boreholes reveal a transition from steady state to seasonal deformation in two shear zones. Since 2020, spring accelerations have intensified in years coinciding with deeper snowpacks and associated melt. These observations, together with statistical modeling, suggest that the shear-band interface is becoming increasingly localized and sensitive to pore-water pressure. Conversely, autumn acceleration is not seen in localized shear zones but manifests as distributed volumetric deformation. Seismic velocity variations within the landslide body also exhibit seasonal patterns that correspond with GNSS velocity, interpreted as changes in landslide rigidity due to water infiltration. This integrated analysis of surface and subsurface data offers new insights into the evolving deformation of Arctic landslides, emphasizing the influence of hydrological forcings on both seasonal and long-term deformation processes.

1 Introduction

In the past decade, many rapid and sometimes catastrophic landslides have occurred in glacial and periglacial environments, including in the high mountains of Asia (Shugar et al., 2021), the Swiss and French Alps (Allen and Huggel, 2013), Scandinavia (Frauenfelder et al., 2018; Kristensen et al., 2021), Iceland (Saemundsson et al., 2007), Greenland (Svennevig et al., 2024; Dai et al., 2025), and Alaska (Patton et al., 2021). The roles of global warming and

https://doi.org/10.5194/egusphere-2026-62
Preprint. Discussion started: 22 January 2026

permafrost degradation are highlighted in these landslides. The long-term analysis of inventories of rapid landslides (meter per second) or displacement rates of slow-moving landslides (millimeters to meters per year) has also shown a statistical increase in landslide activity over time at a regional scale in the Himalayas (Pei et al., 2023) and in northern Scandinavia (Penna et al., 2023a).

The processes linking global warming to landslide activity are complex (Patton et al., 2019), involving a combination of ice loading history (Grämiger et al., 2017; Lacroix et al., 2022; Walden et al., 2025), rapid snowmelt or extreme rainfall events (Ben-Yehoshua et al., 2022), and increased permafrost thaw (Donnini et al., 2023; Cardinali et al., 2000; Gruber and Haeberli, 2007; Hilger et al., 2021). These conditions are becoming increasingly common due to the rising average global temperature, which drives extreme weather events, especially in the Arctic (Rantanen et al., 2022). The combination of all these factors makes it challenging to quantify their individual roles in landslide dynamics. As such, predicting landslide activity in the Arctic in the context of global warming is highly uncertain.

In recent years, several analyses of geophysical datasets over slow-moving landslides have shown the complexity of landslide dynamics (Lacroix et al., 2020), including the role of fluids on pore-water pressure (Iverson, 2000), dilatancy (Iverson, 2005), seepage forces and joint corrosion (Aspaas et al., 2024), progressive damage at the shear-band surface (Bontemps et al., 2020), and fracturing of the moving mass during its long-term motion (Lacroix et al., 2022). All these processes can drive landslide acceleration, exhibiting either seasonal patterns or runaway until system-size rupture (Handwerger et al., 2025). In Arctic landslides, where changes in precipitation and permafrost conditions are expected to vary significantly over the coming years (Patton et al., 2019), these different processes have been little quantified.

The objective of this study is to analyze the driving mechanisms responsible for acceleration phases and, consequently, the potential triggers of catastrophic collapses in Arctic landslides situated near the permafrost boundary. We examine a unique long-term dataset from two neighboring Arctic landslides in Norway, one of which has been equipped with intensive surface and borehole monitoring for twelve years. This dataset enables an in-depth investigation of internal geological and external climatic factors contributing to slope instability in Arctic environments.

2 Data and Methods

2.1 Geological Setting

The Jettan and Gámanjunni landslides are located in Troms County, Northern Norway (Figure 1). The topography surrounding the landslides exhibits a rounded relief with erosional (e.g., paleo) surfaces on the plateaus and long, U-shaped valleys formed during the Quaternary glaciations. The lithology in the area belongs to the Caledonian thrust sheets, specifically the Kåfjord and Vaddas nappes (Andresen, 1988). Table 1 provides a comparative overview of the properties of the two landslides.

https://doi.org/10.5194/egusphere-2026-62
Preprint. Discussion started: 22 January 2026

Table 1. Comparison between the two landslides

	Inferred thickness	Size of instability	Mean slope angle	Orientation	Geology	Velocity (GNSS)	Altitude (meter above sea level)
Jettan landslide	45 to 80 meters depth in boreholes	6 million m^3	30°	W	Garnet-quartz micaschist with amphibole-rich layers, and alternating calc-silicate gneiss and calcitep marble	Mean 8.1 mm/yr (2021-2025)	650 to 400
Gámanjunni landslide	~100 meters depth (SLBL* modeled)	25 million m^3	32°	WSW	Alternating biotite and muscovite micaschist	Mean 27.9 mm/yr (2021-2025)	1100 to 640

*Sloping Local Base Level (SLBL)

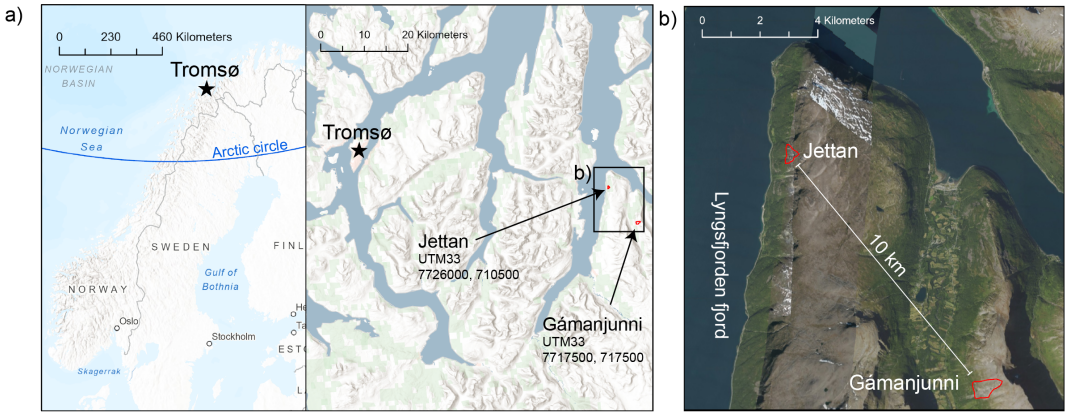

Figure 1. Location of the two landslides, Jettan and Gámanjunni, with their UTM33 GPS coordinates (69° 33'25.7"N, 20° 24'38.5"E, and 69° 28'50.8"N, 20° 34'10.2"E, respectively). a) Map of Scandinavia, the Arctic Circle, and the location of the landslides east of the city of Tromsø (Credit: Esri). b) A zoom-in of the two landslides highlights their spatial distance of less than 10 km (Credit: Kartverket).

2.1.1 Jettan Landslide

The Jettan active landslide is situated along the Lyngsfjorden fjord and is one of several landslides on the Nordnesfjellet's west-facing slope (Figure 2). It slides at an average velocity of up to 12 mm/yr along an average slope of 30°, and includes cliffs of up to 40 meters in height (Braathen et al., 2004). The landslide extends from approximately 200 to 900 meters above sea level and is bounded by two active back-scarp fractures. The volume of the active landslide is estimated to be six million cubic meters (Blikra et al., 2015). The annual theoretical probability of failure has been estimated to be between 1/100 and 1/1000 (NGU, 2025; NVE, 2024; Hermanns et al., 2013). If it fails abruptly, it could cause a devastating tsunami in the fjord below.

https://doi.org/10.5194/egusphere-2026-62
Preprint. Discussion started: 22 January 2026

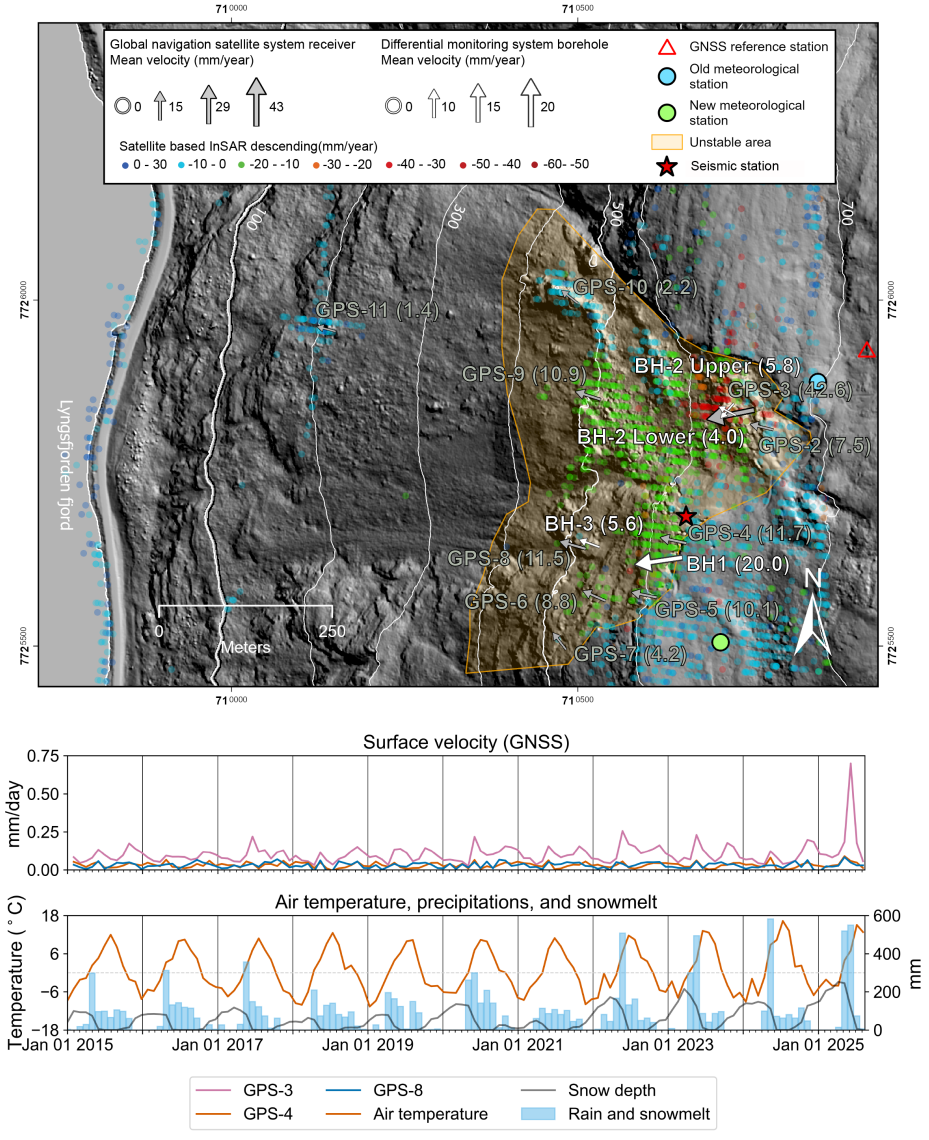

Figure 2. Map of the Jettan landslide showing key morphological features and instrument locations (Credit: Kartverket). Gray arrows represent mean surface velocities (mm/yr) derived from GNSS data, while white arrows indicate borehole displacements from the differential monitoring system (BH), both averaged over the period from 01.01.2021 to 12.08.2025. Arrow dimensions are scaled proportionally to velocity magnitude, with values annotated in parentheses. Borehole BH-2 displays two arrows corresponding to distinct shear zones. White contour lines denote 100-meter elevation intervals. Time series plots include GNSS-derived surface velocities and meteorological parameters over the past decade, smoothed using a 30-day median for GNSS and 30-day cumulative sums for rainfall and snowmelt.

https://doi.org/10.5194/egusphere-2026-62
Preprint. Discussion started: 22 January 2026

The rocks consist of garnet-quartz-mica schists with amphibole-rich layers in the lower parts of the front of the landslide and layers of alternating calc-silicate gneiss and calcite marble in the uppermost part of the landslide of the Nordmannvik Nappe (Zwaan et al., 2006; Skrede, 2013). The nappe unit exhibits high strain and several internal thrust faults. The Jettan landslide is located within one of these faults (Andresen, 1988). The rocks display a distinct foliation dipping approximately 20° towards the west, and two dominant fracture sets are striking NE-SW and ESE-WNW (Braathen et al., 2004; Skrede, 2013; Vick et al., 2021). The back-scarp is approximately 750 m long, starting in the north with a 100 m high cliff segment, then gradually reducing to sinkhole lineaments in the middle, and further steep slopes on the south side. Several geological sub-units show evidence of ductile deformations, such as garnet-quartz-mica schist with blastomylonites and calc-silicate gneiss lenses that contain boudins of amphibole and calcite marble up to tens of meters long (Skrede, 2013). Electric resistivity and refraction seismic data suggest that the rocks are fractured to approximately 50 meters depth and indicate possible sporadic permafrost (Rønning et al., 2008). Temperature measurements in three 100-meter-deep boreholes within the landslide display positive temperatures ranging from 2° to 4° Celsius. In contrast, measurements from temperature sensors in the open back-fracture adjacent to borehole BH-1 indicate subzero rock-wall temperatures during parts of the year and the presence of multi-year ice at the fracture bottom (Blikra et al., 2015), despite the landslide being located below the modeled permafrost boundary (Magnin et al., 2019).

Drill core logs show narrow shear zones in the boreholes. In two out of three boreholes, clays have been detected in the shear zone (Ganerød, 2013, 2014). Analyses of optical televiewer data show that the entire borehole contains fractures. In all boreholes, fractures at the depth of the shear zone dip westward towards the fjord, with angles of approximately 15° in boreholes BH-1 and BH-3 and between 55° and 75° in BH-2 (Elvebakk, 2013, 2014).

2.1.2 Gámanjunni Landslide

The Gámanjunni landslide lies within the Manndalen valley, which contains several landslides and large rock avalanche deposits along its west-facing mountain slope (Figure 3). It slides at an average velocity up to 40 mm/yr, on an average slope of 33°. The landslide consists of a large fractured block that extends from approximately 640 to 1100 meters above sea level and is bounded by the back-scarp, which consists of two surfaces forming a wedge. The volume of the landslide is estimated to be 25 million cubic meters (Böhme et al., 2016b). The annual theoretical probability of failure is more than 1/100 (Geological Survey of Norway (NGU), 2025; NVE, 2024; Hermanns et al., 2013). When failing catastrophically, the landslide could potentially dam the river below, which may cause a devastating flood if this dam were to fail.

The rocks consist of micaschist from the Kåfjord Nappe, characterized by a higher proportion of biotite than muscovite, with amphibole-rich layers and lenses. One of the internal thrust faults from the nappe unit is located in the valley below the Gámanjunni landslide (Böhme et al., 2016b; Quenardel and Zwaan, 2008). There are two fracture sets in the area, striking WNW-ESE and NE-SW. The foliation is dipping on average 8° towards 312°. The back-scarp is dipping on average 51° towards 217° on one side and 58° towards 305° on the other side. The surfaces are

https://doi.org/10.5194/egusphere-2026-62
Preprint. Discussion started: 22 January 2026

very well developed and show progressive failure of rock bridges between the foliation layers (Böhme et al., 2016a). Electric resistivity data suggest an approximate thickness of 10 to 20 meters of highly fractured rocks (Böhme et al., 2016a). The landslide lies above the modeled permafrost boundary (Magnin et al., 2019), and potential permafrost extent ranges from small areas near the top plateau (Böhme et al., 2016a), down to elevations of about 800 meters above sea level, and may include a subsurface layer thickness of 30–50 meters within the landslide mass (Hauck, Christian and Hilbich, Christin, 2018; Etzelmüller et al., 2022).

2.2 Geophysical Monitoring and Processing

The Norwegian Water Resources and Energy Directorate (NVE) manages the early warning systems for the two landslides. The Jettan and Gámanjunni landslide monitoring systems have been improved over time with several instruments added over the years. The Jettan landslide dataset consists of a wide range of instruments that measure displacement, groundwater level, seismic activity, and meteorology (for additional information, see Table A1). The Gámanjunni landslide dataset is limited to surface displacement and meteorological data, with no borehole or seismic measurements available to constrain subsurface conditions (for additional information, see Table A2). Borehole installations at the Jettan landslide site proved technically challenging, while at the Gámanjunni site, drilling was not undertaken due to prohibitive costs.

2.2.1 Surface Displacement Data

The Global Navigation Satellite System (GNSS) sensors are spatially distributed on the two slopes, with ten and eight instruments for the Jettan and Gámanjunni landslides, respectively. For both landslide sites, relative positioning is employed using a reference GNSS receiver located on stable ground, within 0.5 km of each landslide. The data are post-processed in 12-hour intervals to derive surface displacements with millimeter-level precision (σ = 0.6 mm), as estimated by Cautus Geo, the company that supplied the Trimble equipment and performed the time series processing. To reduce the noise associated with height measurements, we utilized the northing and easting components to construct two-dimensional displacement vectors. At the Gámanjunni landslide site, the initial reference receiver was not installed on stable ground, which rendered the data unreliable, while the subsequent reference station was affected by ice accumulation that degraded the signal from 28.12.2021 to 07.02.2022. Consequently, only data acquired with the new reference station, after removing the period during which the antenna was iced, are included for the analysis.

2.2.2 Borehole Displacement and Hydrologic Measurements at the Jettan Landslide

Four boreholes were cored and logged, three of which are currently instrumented with a Differential Monitoring System (DMS) supplied by the company Geoengineering Service Center. These instruments are calibrated and tested before installation (Foglino et al., 2015). The boreholes BH-1, BH-2, and BH-3 are named according to the

https://doi.org/10.5194/egusphere-2026-62
Preprint. Discussion started: 22 January 2026

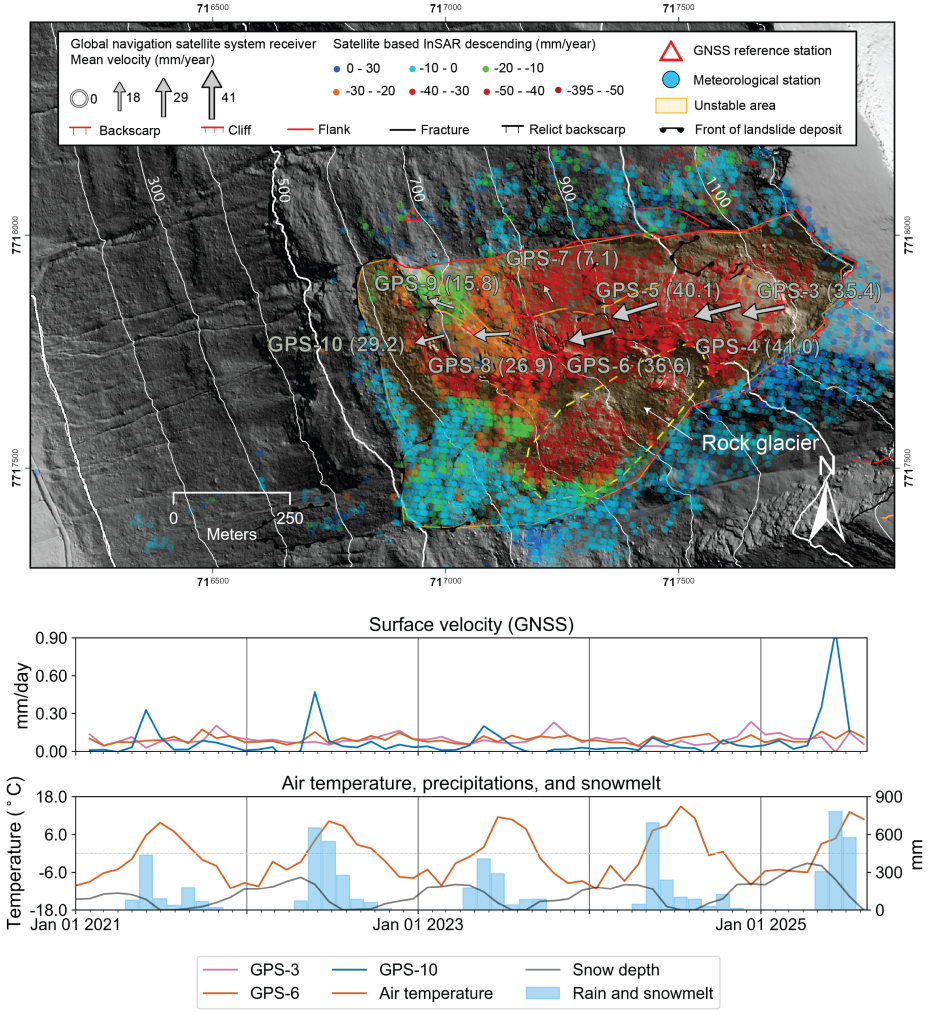

Figure 3. Map of the Gámanjunni landslide illustrating morphological features and instrument locations (Credit: Kartverket). Gray arrows denote mean GNSS-derived surface velocities (mm/yr) calculated for the period from 01.01.2021 to 12.08.2025, with arrow size scaled to velocity magnitude and annotated values in parentheses. The yellow dashed outline delineates the active rock glacier extent. Elevation contours are shown in white at 100-meter intervals. Accompanying plots display GNSS velocity and meteorological time series over the past five years, smoothed using 30-day median for GNSS and 30-day cumulative sums for rainfall and snowmelt.

order of instrumentation, with BH-1 drilled and instrumented first (Table A3). The DMS 2D Rock system was installed in a plastic borehole casing containing strings of one-meter biaxial inclinometers extending to a depth of approximately 100 meters. A piezometer was placed near the bottom in each borehole, and all sensors record measurements at hourly intervals. The movement of the landslide gradually induces deformation of the boreholes,

https://doi.org/10.5194/egusphere-2026-62
Preprint. Discussion started: 22 January 2026

130 which will ultimately lead to instrument failure. While deforming, we obtain displacement in millimeters in the north-south and east-west directions. Data are downloaded from the software DMS EW (CSG, 2007). We analyze the entire time series of the boreholes, i.e., 11-year-long (BH-2 and BH-3) and 12-year-long (BH-1) series.

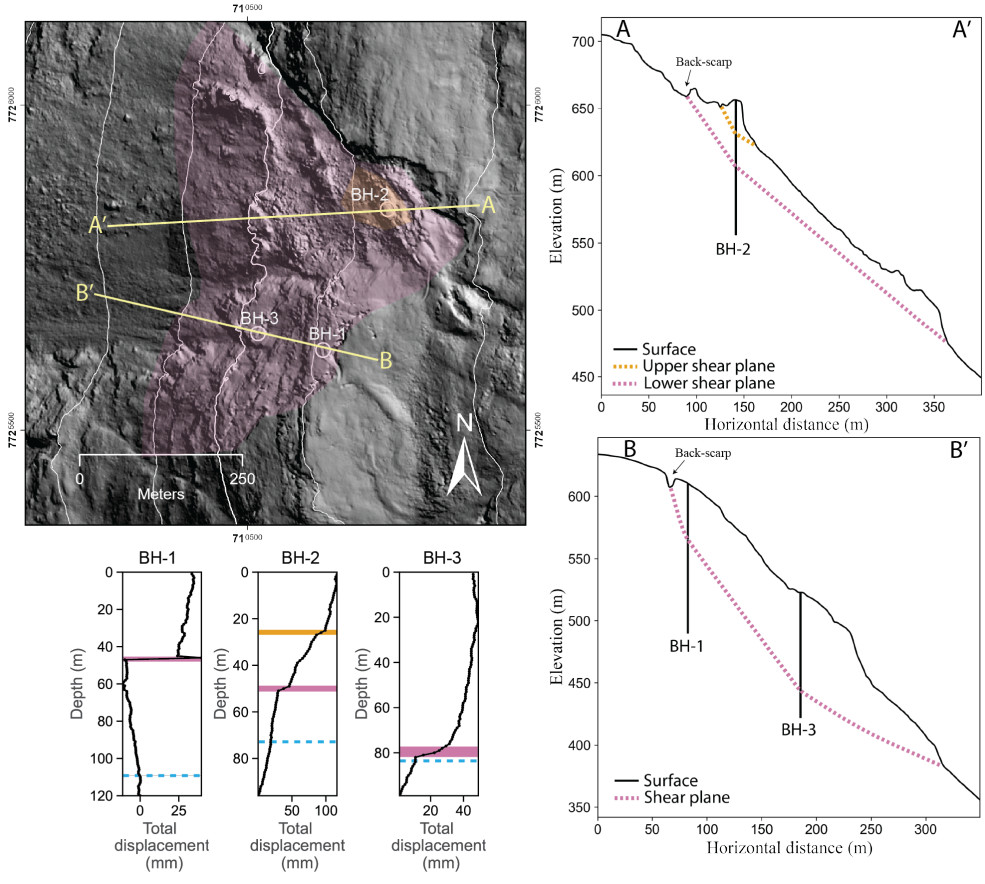

Figure 4. Schematic representation of the Jettan landslide based on identified shear zones detected in the boreholes. The two profiles A-A' and B-B' and their associated boreholes (BH-1 to BH-3) are shown on the map (Credit: Kartverket). The displacement in the three boreholes indicates the presence of one or two distinct shear zones. The scale of the axes differs between each plot. The displacement is measured in the slip direction and represents the maximum displacement recorded in each borehole. The orange and pink lines represent the upper and lower shear zone locations, and the dashed blue line represents the maximum water level. We interpreted the shear zones by plotting the boreholes on the profiles and extrapolating the shear zones to mapped morphological structures. Proposed sliding scenarios are represented spatially on the map with transparent orange and pink polygons.

https://doi.org/10.5194/egusphere-2026-62
Preprint. Discussion started: 22 January 2026

2.2.3 Surface Broadband Seismic Station Data at the Jettan Landslide

Monitoring apparent surface wave velocity provides insights into the variations of the mechanical characteristics of the subsurface. Velocity variations are caused by changes in rigidity (the shear modulus), density, pore water pressure and temperature (Le Breton et al., 2021b). In the case of mountain and arctic regions, temperature has also been proposed to be a driving mechanism of seismic velocity variation through icing/de-icing effects at surface and permafrost decrease (Albaric et al., 2021).

The variation of apparent surface wave velocity (dv/v) inside the landslide between 2016 and 2025 was computed using single-station correlation of ambient seismic noise (Hobiger et al., 2014) at station JETT, which is operated by the Norwegian Seismic Array (Norsar, 1971). A complete description of the processing is provided in Appendix (A1). The station is a 3-component CMG broadband velocimeter operating at a frequency of 200 Hz. For each of the three possible pairs of components (Vertical-North, Vertical-East, and North-East), data were cut into 1-hour-long time series. They were standardized, filtered between 1 and 50 Hz, and then whitened in the same frequency range to set its spectral amplitude to 1. The data were cross-correlated, and the daily correlogram was computed as the average of the 24 hourly correlograms. Velocity variations were computed using the stretching technique (Sens-Schönfelder and Wegler, 2008; Hadziioannou et al., 2009). First, the three matrices of daily correlograms were denoised using a singular value decomposition Wiener filter (Moreau et al., 2017), with a filter size of 7 in both dimensions (days and lag), and a number of singular values of 20. A reference correlogram was computed (the average of the 2543 available daily correlograms), and each daily correlogram was stretched and compared to the reference. Stretching was conducted in the lag range of [-2 : -0.2] and [0.2 : 2] seconds and in the frequency range 3-8 Hz (see Section 2.2.5). This lag range corresponds to the near coda, away from ballistic waves, and is therefore less sensitive to source variability. Eventually, dv/v was computed as the average of the three dv/v time series, weighed by their coefficient of correlation (Hobiger et al., 2014). The coefficient of correlation quantifies the similarity between the reconstructed waveforms, where a low coefficient (strong decorrelation) is associated with structural changes and also fluid injection into the subsurface (Larose et al., 2015; Le Breton et al., 2021a).

2.2.4 Meteorological Data

The meteorological station at the Jettan landslide was installed in 2014 above the back scarp (blue circle in Figure 2). Due to its location on an inclined slope next to other buildings, which influenced the measurements, a new meteorological station was installed further south above the back scarp in 2022 (green circle in Figure 2). For the Gámanjunni landslide, the meteorological station was installed on the plateau above the landslide in 2017 (blue circle in Figure 3). For comparing the Jettan and Gámanjunni landslides, we utilized seNorge data (seNorge, 2024) for all meteorological parameters at both sites. This approach was chosen because the meteorological station on Gámanjunni is located 200 meters above the landslide, and snow measurements at Jettan contain significant gaps. The modeled variables were provided at the elevation of each landslide, ensuring a fair comparison. seNorge is a weather model

https://doi.org/10.5194/egusphere-2026-62
Preprint. Discussion started: 22 January 2026

service provided by the Norwegian Water Resources and Energy Directorate, Norwegian Meteorological Institute, the Norwegian Public Road Administration, and the Norwegian Mapping Authority. The model utilizes all approved meteorological stations in Norway, including the landslide stations, to provide 1 km grid cells of daily interpolated meteorological data that are locally weighted (seNorge, 2024; Lussana, 2021). The relocation of the Jettan weather station improves snow accumulation measurements, which could bias the long-term trends of modeled meteorological variables. In addition to surface temperature, precipitation, snow depth, and snowmelt and rain from the seNorge model, we have modeled ground temperatures at 1 meter, 45 meters, and 115 meters depth by using the CryoGrid community model (Westermann et al., 2023). Details of the model setup are provided in the Appendix (A2).

2.2.5 Integration of Data

We utilized ArcGIS software (ESRI, 2023) to visualize the displacement data spatially. The 1-meter digital elevation models were downloaded from Høydedata (Høydedata, 2024) for both landslides and were used to plot altitude contours and create topography profiles, enabling evaluation of failure scenarios.

To delineate periods of expected ground freezing and thawing, we derived a freeze index, which is the monthly ratio of days with mean air temperatures above 0°C to those below 0°C. Freeze index values above one indicate more days above 0°C, while values below one indicate more days below 0°C.

To calculate the total displacement in the borehole, it is necessary to sum the displacements recorded by all the inclinometers (Aspaas et al., 2024; Ruggeri et al., 2020). We obtained the maximum displacement in the slip direction for each inclinometer by calculating the maximum amplitude and its orientation. We extracted displacement components in the north and east directions, calculated the magnitude and mathematical azimuth, and then converted the azimuth to compass bearings. Then, we plotted the cumulative displacement of the borehole and identified zones of increased displacement, i.e., the shear zones (Figure 4). A few electrical or technical errors on the borehole instruments have been resolved by remote resets of the modules, resulting in the displacement being reset to zero. We have resolved these incidents by raising the displacement to the previous level, with a one-day median difference before and after the reset. In addition, we removed a few abrupt, significant spikes in the time series due to lightning strikes.

We filtered the GNSS and borehole time series using a coarse outlier removal of three standard deviations, followed by a linear interpolation to fill data gaps and a Savitzky-Golay filter (SciPy Developers, 2025) in combination with a 14-day centered rolling median filter (Pandas Developers, 2025b). To estimate the sliding velocity, we calculate the slope of a centered rolling linear regression of the filtered displacement time series. For each time step t, we consider a symmetric window of W days centered on t, and fit a straight line to the displacement values within the window. The slope of this line $v(t)$ represents the velocity at time t:

$$v(t) = \frac{\sum_{i=1}^{W}(x_i - \bar{x})(y_i - \bar{y})}{\sum_{i=1}^{W}(x_i - \bar{x})^2}, \tag{1}$$

where we compute the local linear regression of displacement y_i against time x_i.

https://doi.org/10.5194/egusphere-2026-62
Preprint. Discussion started: 22 January 2026

Temporal aggregation of the time series was performed using the resample method (Pandas Developers, 2025a). A centered rolling window was applied to compute running sums of meteorological variables (Pandas Developers, 2025b). Centering the rolling window minimizes time-lag effects across different window lengths, as illustrated in Figure A1.

To analyze structural changes within the landslide, we evaluated the sensitivity of seismic surface waves with depth and frequency to obtain the correct frequency range, scanning the entire unstable mass. To achieve this, a vertical velocity model was defined using data available for the site (Blikra and Christiansen, 2014; Vick et al., 2021; Rønning et al., 2008), and empirical relationships (Brocher, 2005b) to evaluate P- and S-wave velocities for missing data. The sensitivity kernels for both Rayleigh and Love waves were computed using the Disba package (Luu, 2021). Results show that the frequency range of 3-8 Hz is suitable for monitoring the active landslide at depths of approximately 10 and 50 m. Details of the seismic velocity model are provided in the Appendix (A2).

To quantify relationships among variables, we first aligned the temporal resolution of the datasets and applied time series filtering without introducing time shifts between series. The data were then scaled using the MinMaxScaler function from the Python package sklearn (scikit-learn developers, 2024) to obtain similar weights across variables. We assessed stationarity using the Dickey-Fuller test (Perktold et al., 2023). Cross-correlation was performed using Spearman rank correlation as it is non-parametric and suitable for time series data, which often violate normality assumptions. Lags analysis was limited to three months to capture seasonal effects, as longer-term correlations across seasons are unlikely to represent causal relationships.

To further develop quantitative relationships between different variables and their explanatory power for the resulting movement in the boreholes, we employed a dynamic regression model, specifically the AutoRegressive Distributed Lags (ARDL) model. This modeling approach allows predicting a time series (i.e., the sliding velocity, called the endogenous variable) using the time series of other variables (i.e., water pressure, rain, or snowmelt, called the exogenous variables). The autoregressive (AR) component of the model accounts for the influence of the endogenous variable's own past values, meaning that yesterday's sliding velocity influences today's sliding velocity. The distributed lag (DL) component captures the delayed effects of the exogenous variables on the endogenous variable, meaning that yesterday's water pressure influences today's sliding velocity. In the ARDL model, each variable can have its own lag order. For example, in a model with sliding velocity and water pressure, sliding velocity may include three lags and water pressure two lags, resulting in a lag structure of (3, 2). Assuming daily data, this means that today's sliding velocity depends on its previous three days and the previous two days of water pressure (Bismans, 2025).

Due to the large size of the dataset, the original ardl_select_order function from the Statsmodels ARDL package (Perktold et al., 2023) was computationally inefficient for determining the optimal lag structure. By optimal lag structure, we mean the best combination of lag lengths for both endogenous and exogenous variables that provides the best model fit. To address this limitation, we revised the function to improve efficiency and enable robust lag selection for endogenous and exogenous variables according to the Bayesian Information Criterion (BIC). BIC

https://doi.org/10.5194/egusphere-2026-62
Preprint. Discussion started: 22 January 2026

discourages overfitting by penalizing model complexity, and lower values indicate better model fit. The lag search was restricted to a maximum of three months under the assumption that all exogenous variables would influence the endogenous variable within that time frame. Since this process is computationally intensive, we down-sampled the time series to weekly intervals. Displacement, groundwater pressure, air temperature, ground temperature, and temporal variation in seismic velocity were mean-averaged, while precipitations were summed.

Once the optimal lag structure was identified, the ARDL model was fitted using the following ARDL function (Perktold et al., 2023):

$$Y_t = \sum_{p=1}^{P} \alpha_p Y_{t-p} + \sum_{k=1}^{M} \sum_{j=0}^{Q_k} \beta_{k,j} X_{k,t-j} + \epsilon_t, \tag{2}$$

where Y_t represents the endogenous variable at time t. The first summation represents the autoregressive component, where past values of Y up to lag P are included, where α_p is the estimated coefficient. The second summation corresponds to the distributed lag component, which accounts for the influence of M exogenous variables. For each exogenous variable X_k, both its current value and lagged values up to Q_k are included, with associated estimated β coefficients for variable k at lag j. The estimated α and β coefficients indicate the magnitude of the variable's effect on the endogenous variable, where a larger absolute value indicates a stronger influence. The term ϵ_t represents the error in the model.

To evaluate the model's predictive performance, we split the selected time series into training and test datasets using a ratio 80-20. To isolate the contribution of the autoregressive dynamics, we also fitted a simplified Distributed Lag (DL) model by setting the lagged endogenous terms to zero. In this configuration, the DL model predicts the endogenous variable solely from current and lagged values of exogenous variables.

This comparison enables an assessment of whether including AR terms improves model performance. We evaluated both models using the BIC score, following the interpretation thresholds in Table 6 of Raftery (1995), and compared their root-mean-squared errors (RMSE) of the out-of-sample test data.

3 Results

3.1 Jettan and Gámanjunni Surface Velocities

At the Jettan landslide, we study the period from 01.01.2015 to 12.08.2025, where the mean rate of horizontal displacement across all GNSS receivers (except GPS-3) is 7.8 mm/yr, varying from 6.3 mm/yr in 2015-2016 to 10.5 mm/yr in 2025. The displacement time series shows a distinct seasonal trend for all GNSS receivers, which is most pronounced at GPS-3 (Figure 2). GPS-3 is situated on a kinematically distinct block that is structurally separated from the main landslide body. As this block moves independently from the main landslide, we excluded it to calculate the mean displacement rate of the landslide. The location of this block is highlighted in Figure 4.

https://doi.org/10.5194/egusphere-2026-62
Preprint. Discussion started: 22 January 2026

At the Gámanjunni landslide, we study the period from 01.01.2021 to 12.08.2025, where the mean horizontal displacement rate for all GNSS receivers is 27.9 mm/yr, fluctuating from 24.4 mm/yr in 2022-2023 to 39.4 mm/yr in 2025. There is a distinct seasonal component in the displacement data, most noticeable at GPS-10 where the frontal lobe of the landslide accelerates in late spring. The seasonality is less pronounced for the other GNSS receivers relative to the Jettan landslide (Figure 3). The mean displacement rate since 2021 is more than three times that of the Jettan landslide. Both Jettan and Gámanjunni display clear seasonal fluctuations in the GNSS data, with peak velocities in late spring and late autumn. For both landslides, we report mean horizontal displacement rates calculated across all GNSS receivers, excluding GPS-3 at Jettan (Figure 5).

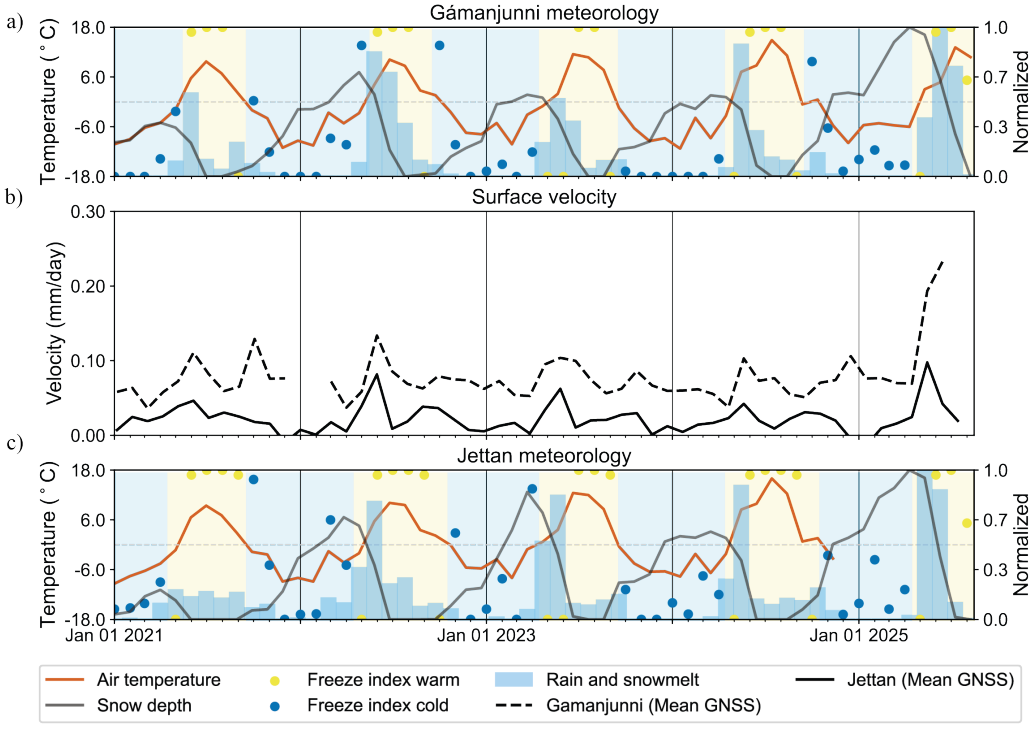

Figure 5. Time series of the air temperature and normalized freeze index, precipitation, and rain and snowmelt are displayed in (a) and (c) for the Gámanjunni and Jettan landslides, respectively. The transparent blue and yellow background highlights cold and warm periods based on the freeze index. The time series of the mean velocity of all GNSS receivers for the Jettan and Gámanjunni landslides (except GPS-3 for Jettan) are shown in (b). All time series have been smoothed by down-sampling to a 30-day median or summation for precipitation and rain and snowmelt.

https://doi.org/10.5194/egusphere-2026-62
Preprint. Discussion started: 22 January 2026

3.2 Borehole Data at the Jettan Landslide

At the Jettan landslide, we compare the cumulative displacement over all inclinometers in the boreholes and the nearest GNSS receivers over the period from 01.01.2020 to 01.01.2024. Borehole BH-1 displays a cumulative displacement of 36.0 mm, while GPS-4 and GPS-5 display 45.5 mm and 39.9 mm, respectively. Borehole BH-2 displays a cumulative displacement of 162.5 mm, while GPS-3 displays 157.3 mm, and borehole BH-3 displays a displacement of 58.8 mm, while GPS-8 displays 45.6 mm (Figure 2). We can detect the shear planes from the cumulative displacement plots in Figure 4. Analysis of the shear planes shows that borehole BH-1 is predominantly concentrated within the localized shear zone, whereas in BH-2 and BH-3, deformation is more broadly distributed and only weakly localized within the sliding zone. When we compare the displacement in sliding zones, we observe that boreholes BH-1 and BH-3 move at a similar rate (5.3 mm/yr) over the period from 2018 to 2020. Borehole BH-2 upper and lower shear zones have a slightly lower displacement rate (3.3 and 4.7 mm/yr). In 2020, borehole BH-1 started accelerating (7.0 mm/yr) and accelerated again in 2022 21.4 mm/yr). During the first acceleration, borehole BH-3 also accelerated (6.3 mm/yr), but slowed down in 2022 (5.6 mm/yr). At the same time as the last acceleration of borehole BH-1, the amplitudes of the seasonality of borehole BH-2's upper shear plane almost doubled (from 3.3 mm/yr in 2019 to 5.6 mm/yr in 2022), and nearly tripled in 2025 (8.7 mm/yr). During this period, GPS-4 and GPS-8, located at boreholes BH-1 and BH-3, continued to move at a steady displacement rate (11.1 ±1 mm/yr from 2018 to 2024). Similarly, the lower shear zone of BH-2 maintained a displacement rate consistent with that of the upper shear zone, but without the seasonal fluctuations (4.3 ±1 mm/yr from 2018 to 2024).

The seasonal trends visible in the GNSS time series of Jettan are harder to spot in the borehole data. A clear seasonal pattern of increased velocity in late spring is pronounced for the upper shear zone in borehole BH-2, and infrequent bursts of slip acceleration occur in boreholes BH-1, BH-2 lower shear zone, and BH-3 (Figure 6).

3.3 Seasonal Variations in Climatic Parameters and Seismic Velocity

Over the ten years from 01.01.2015 to 12.08.2025 at the Jettan landslide and the four years from 01.01.2021 to 12.08.2025 at the Gámanjunni landslide, the daily average median air temperature was 0.2°C at Jettan, with a maximum of 23.9°C in 2018 and a minimum of -18.9°C in 2016, and -1.8°C at Gámanjunni, with a maximum of 19.6°C in 2022 and minimum of -19.0°C in 2024. Modeled ground temperatures at borehole BH-1 (see Section 2.2.4, Appendix, A2) provided long-term trends beyond the borehole measurement period. The simulated mean annual ground temperature (MAGT) at 1 meter depth over the last decade (2015-2025) was 2.4°C, reflecting the thermal offset relative to air temperature. The model shows positive MAGT at both 45 m and 115 m depths, indicating that no permafrost is present within the landslide body, which is consistent with recent borehole observations. Over the last 50 years, the simulated MAGT at 1 meter depth increased by 0.2°C per decade.

The freeze index for the two landslides shows shorter warm periods compared to cold periods for the Gámanjunni landslide on average, with a median of 0.51 ranging from 0.11 (2023) to 0.61 (2025), while the Jettan landslide has

https://doi.org/10.5194/egusphere-2026-62
Preprint. Discussion started: 22 January 2026

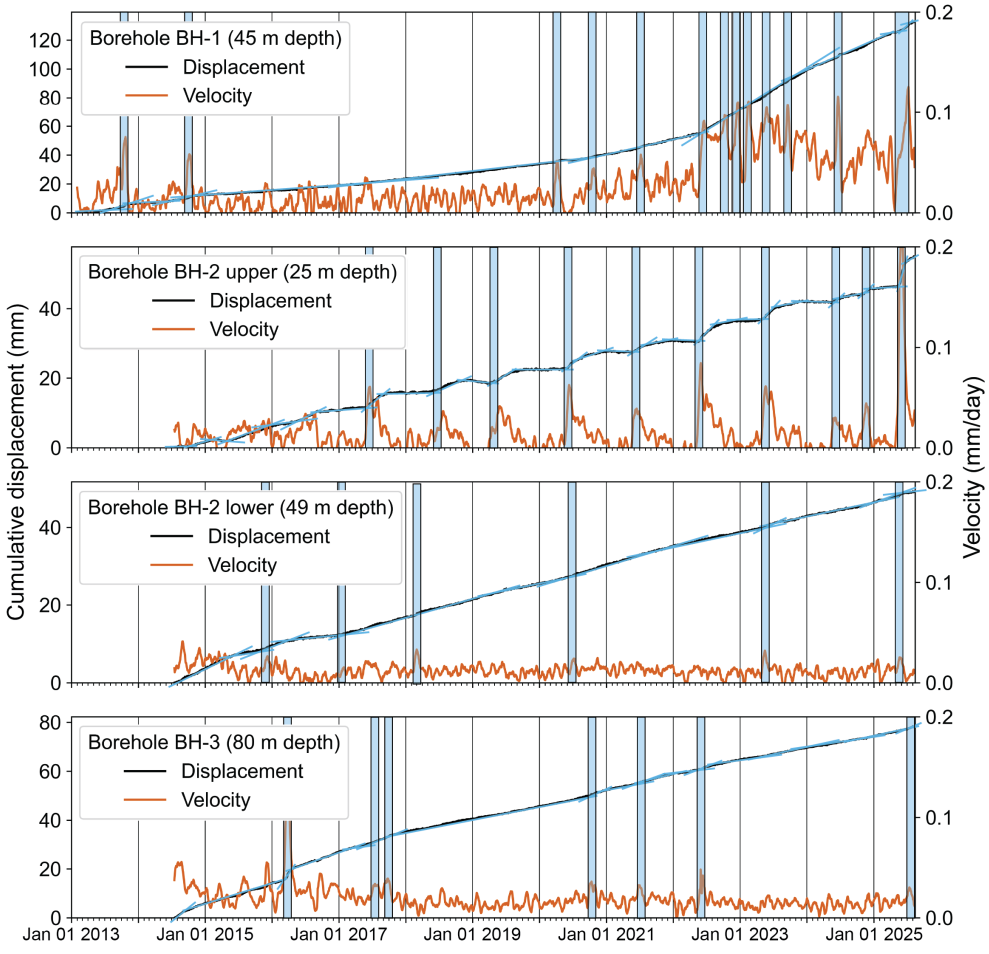

Figure 6. Time series of cumulative displacement (black) and velocity (orange) in the Jettan landslide. Data are measured in the shear zone inclinometers of borehole BH-1 (a), the two shear zones of borehole BH-2 (b and c), and the shear zone of borehole BH-3 (d) are presented. Blue linear trend lines are overlaid on the displacement curves, and shaded blue rectangular boxes indicate periods of acceleration.

similar durations of warm and cold periods on average with a median of 1.24 ranging from 0.57 (2023) to 1.43 (2024) over the period from 01.01.2021 to 12.08.2025 (Figure 5).

The median yearly rain and snowmelt is 940 mm, ranging from 659 mm in 2021 to 1254 mm in 2022 for the Jettan landslide area, and 1324 mm, ranging from 905 mm in 2021 to 1700 mm in 2022 for the Gámanjunni area. At the Jettan landslide site, water pressure recorded in borehole BH-1 consistently indicates minimal or absent pore pressure. In contrast, borehole BH-2 exhibits pronounced seasonal variations of up to 17 meters, with peak levels

https://doi.org/10.5194/egusphere-2026-62
Preprint. Discussion started: 22 January 2026

occurring in spring and remaining elevated throughout the year. Borehole BH-3 shows a similar timing of the peak, but with a smaller amplitude of up to 5 meters, followed by a sharp decline in water level (Figure A2).

The relative seismic velocity variation (dv/v) exhibits a recurring seasonal pattern. It drops every spring and reaches two distinct minima below the two standard deviation threshold, one in summer and another in autumn. The signal then gradually recovers to near-baseline levels in mid-winter before the cycle begins again in spring (Figure 7). For the period from 01.01.2016 until 31.07.2025, the dv/v trend is decreasing by -0.23% per year (Figure A3).

3.4 Controlling Parameters of Landslide Velocity

3.4.1 Surface Displacement of the Jettan and Gámanjunni Landslides

Analyzing the time series from 01.01.2021 to 12.08.2025, based on 30-day mean velocity of all GNSS receivers (excluding GPS-3 at Jettan), reveals a moderate correlation between the two landslides (Pearson's r =0.49). On average, acceleration at Jettan precedes that of Gámanjunni by 17 days. The main differences between the two landslides are highlighted in Table 1. Focusing on the year 2022, the GNSS velocity at the Gámanjunni landslide shows a lag of approximately 20 days after peak rain and snowmelt when using a 14-day running sum, with a moderate to strong correlation (Pearson's r =0.52) during spring. At the Jettan landslide, the lag is about two days, with a strong correlation (Pearson's $r = 0.71$). From September to December, after snowmelt has ceased, we observe no lag with a strong correlation between rain events and velocity increases for the Jettan landslide (Pearson's $r = 0.69$). No comparable relationship is evident for the Gámanjunni landslide during this period.

3.4.2 Correlation of Borehole Accelerations with Groundwater Pressure, Climatic Parameters, and Changes in Seismic Velocities

The 30-day slip velocity of the spring accelerations in the upper shear zone of borehole BH-2 and the changes in its water table display a strong correlation (Pearson's r =0.74) with a 5-day lag for the year 2022. The 2022 acceleration in borehole BH-1 and the upper shear zone in borehole BH-2 shows a moderate to very strong correlation between the 30-day velocity and the 14-day running sum of rain and snowmelt (Pearson's r =0.36 and 0.79), where the borehole velocity lags are 23 and 4 days, respectively. There is a very strong negative correlation with the drop in dv/v and the slip acceleration in borehole BH-1 and BH-2 upper shear zone (Pearson's coefficients r =-0.80 and -0.90), where the dv/v lags are 30 and 68 days for the year of 2022. The rain and snowmelt, as well as ground temperature (1 meter depth), also display a strong and very strong negative correlation with the dv/v (Pearson's r =-0.74 and -0.98), with a dv/v lag of 75 and 49 days for the year 2022, respectively. The water pressure in borehole BH-2 upper shear zone and dv/v lag 60 days with a strong correlation (Pearson's r =-0.86). These trends persist throughout the entire time series of accelerations for borehole BH-2 upper shear zone, but are not observed for borehole BH-1.

https://doi.org/10.5194/egusphere-2026-62
Preprint. Discussion started: 22 January 2026

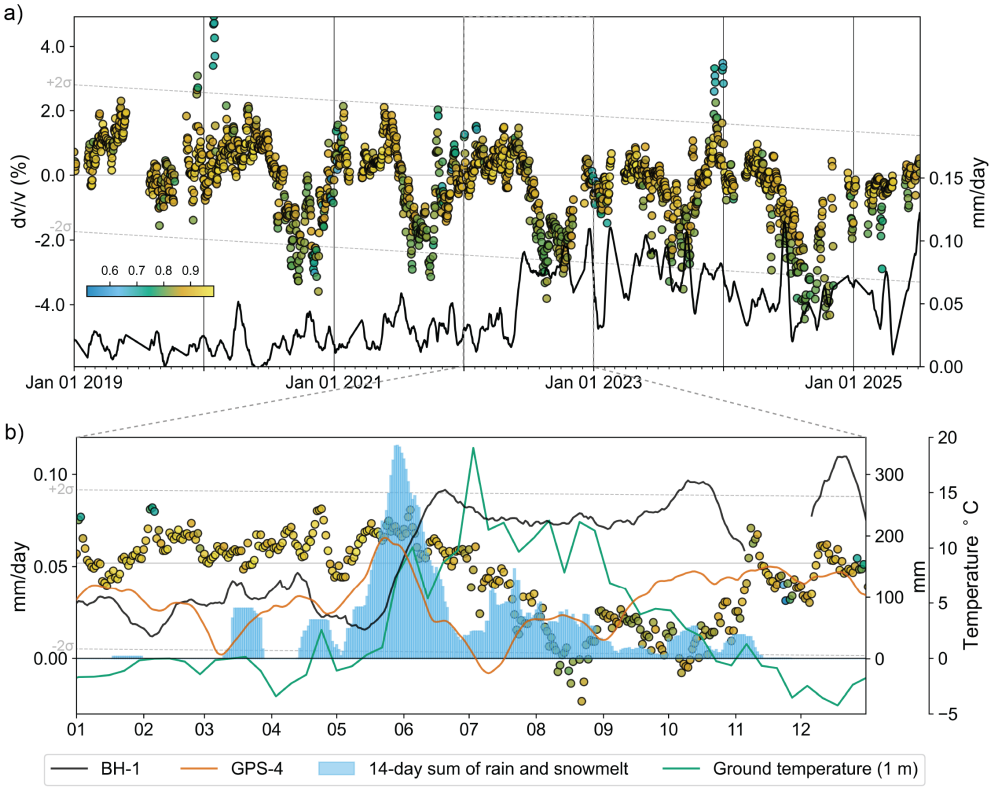

Figure 7. a) The apparent surface velocity variations (dv/v) with annual amplitude and long-term trend in the Jettan landslide, colored by cross-correlation values, and slip velocity recorded in borehole BH-1 (black line). The stippled gray lines represent ± two standard deviations of dv/v around the linear trend over the full period. A seasonal drop below this threshold has been evident since 2020. b) Detailed view of 2022 showing correlations between dv/v and seasonal accelerations in borehole BH-1, mean GNSS velocity, the 14-day running sum of rainfall and snowmelt, and modeled weekly ground temperature at 1 meter depth.

3.4.3 ARDL Models of the shear Zone in Borehole BH-1 and the upper shear Zone in Borehole BH-2

We applied AutoRegressive Distributed Lags (ARDL) models (see Eq. 2) to examine how shear zone slip velocity (endogenous variable) responds to borehole measurements and meteorological factors (exogenous variables) between 01.01.2019 to 31.07.2025.

For borehole BH-2 (upper shear zone), the model included one endogenous (slip in BH-2) and four exogenous variables: groundwater pressure from BH-2, air temperature, rain and snowmelt, and apparent seismic velocity change (dv/v), using weekly data with up to 13 lags. The optimal lag structure, selected by the BIC criterion, was

https://doi.org/10.5194/egusphere-2026-62
Preprint. Discussion started: 22 January 2026

(3,0,0,0,0) (see Section 2.2.5). This means that the current displacement depends strongly on its own past values (lags 1 to 3) and is immediately influenced by ground water pressure, precipitation, air temperature and dv/v (lag 0). The estimated α and β coefficients for these terms are shown in Table A4.

For borehole BH-1, the model considered one endogenous (slip in BH-1) and six exogenous variables: displacement and groundwater pressure from borehole BH-3, air temperature, ground temperature (1 meter depth), rain and snowmelt, and dv/v. The optimal lag structure was (8,0), meaning that BH-1 displacement is primarily controlled by its own history (lags 1-8) and responds immediately to BH-3 displacement (lag 0). The estimated α and β coefficients for these terms are shown in Table A5).

To evaluate the role of autoregressive dynamics, we compared the full ARDL models with reduced distributed lag (DL) models that exclude past values of the endogenous variable. The ARDL models outperformed DL models, with lower BIC values (BH-2 upper shear zone: -973 vs. -967, and BH-1: -375 vs. -128, (Raftery, 1995)) and 37% and 43% lower out-of-sample root mean squared error, indicating substantially improved predictive accuracy. Only statistically significant variables ($p<0.05$) were included in the final models. Observed and predicted velocities for BH-1 and BH-2 (upper shear zone) are shown in Figure 8.

4 Discussion

4.1 Kinematics of the Jettan and Gámanjunni Landslides

Numerous landslides in Arctic and high-alpine environments have been linked to permafrost degradation, including cases in Alaska (Patton et al., 2021), Greenland (Svennevig et al., 2024; Dai et al., 2025), the Swiss and French Alps (Allen and Huggel, 2013), and Norway (Frauenfelder et al., 2018; Kristensen et al., 2021). In Northern Norway, landslide velocities have been shown to correlate with temperature, suggesting a widespread influence of permafrost thawing on slope stability (Penna et al., 2023a).

To better understand landslide driving mechanisms in Arctic settings, we compare the kinematics of the Jettan and Gámanjunni landslides. For each site, we compute the mean horizontal displacement across all GNSS receivers to highlight overall kinematic trends and reduce noise, acknowledging that this approach does not capture local variations. Both landslides exhibit similar seasonal patterns: accelerations in spring and autumn, reduced velocities in summer, and a minimum in winter (Figure 5). Velocity signals are strongly correlated, with Jettan's peak spring acceleration occurring approximately 17 days earlier than Gámanjunni's. The following discussion examines the similarities and differences between the landslides.

At Jettan, spring slip velocities exceed those in autumn, whereas Gámanjunni shows a less consistent pattern, with some years exhibiting higher autumn accelerations. These accelerations correlate strongly with water availability, as indicated by responses to rain and snowmelt in both seasons, suggesting hydrological forcing as a key driver of short-term dynamics. This interpretation aligns with established links between infiltration, groundwater pressure, and landslide displacement (Iverson and Major, 1987). Subsurface thermal conditions differ markedly between the two

https://doi.org/10.5194/egusphere-2026-62
Preprint. Discussion started: 22 January 2026

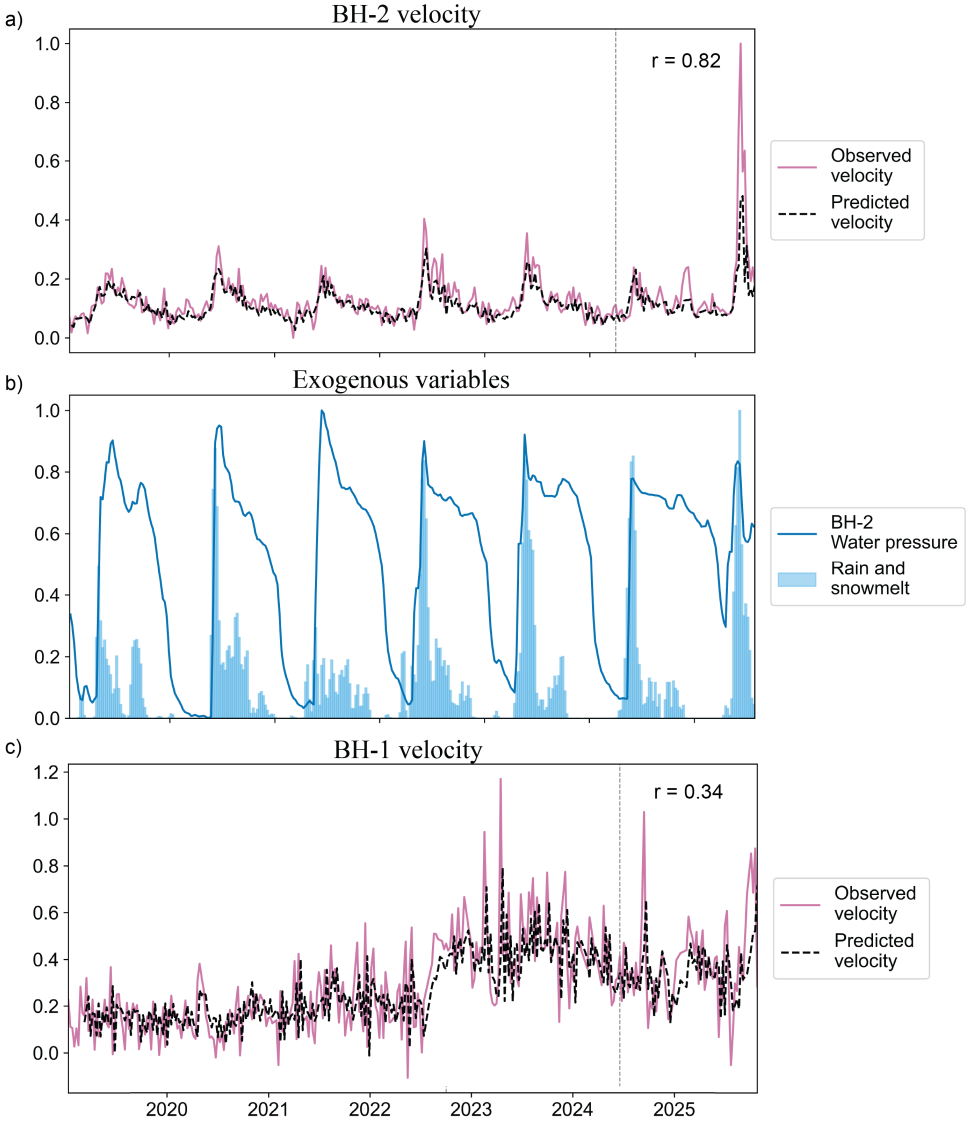

Figure 8. Time series of the analyzed period of the models. Panel a) shows the observed and predicted borehole BH-2 velocities in the upper shear zone. Panel b) shows the exogenous variables contributing to the prediction of BH-2. Panel c) displays the observed and predicted velocities within the shear zone of borehole BH-1. All data are normalized. The vertical dashed line in both plots marks the division between the 80% training (modeled) and 20% testing (predicted) periods, and the correlation coefficients shown for the predicted segment.

sites. At Gámanjunni, discontinuous permafrost is inferred from temperature sensors and geophysical observations. Etzelmüller et al. (2022) proposed that spring accelerations may result from meltwater input from ice and snow in fractures. During colder climatic periods, such as the Little Ice Age, permafrost formation at the Jettan landslide was

https://doi.org/10.5194/egusphere-2026-62
Preprint. Discussion started: 22 January 2026

likely (Czekirda et al., 2023). At present, however, the landslide lies below the regional mountain permafrost limit, and evidence from temperature sensors, borehole measurements, and CryoGrid modeling indicates that permafrost is absent. Nevertheless, multi-year ice persists within the backscarp, which may influence hydrological processes by delaying and amplifying infiltration as it melts (Pogrebiskiy and Chernyshev, 1977; Blikra and Christiansen, 2014).

In autumn, infiltration is lower than in spring because snow has melted. Increased slip velocity in autumn correlates with rain events at Jettan, while the relationship is more complex at Gámanjunni. Air temperature and permafrost cooling may influence autumn velocities, as maximum temperature is critical for rock glaciers deformation (Kääb and Røste, 2024) and likely for landslides affected by permafrost (Gruber et al., 2004; Ravanel et al., 2017). Notably, in some years, the annual peak velocity occurs in autumn, suggesting that permafrost may influence seasonal acceleration (Figure 5).

The Gámanjunni landslide moves three times faster than Jettan. Several factors may contribute to this difference, including geological structural characteristics, slope angle (29° at Jettan and 32° at Gámanjunni), and ground thermal conditions. The landslides occur in different lithological units: Jettan lies within the Nordmannvik Nappe, whereas Gámanjunni is in the Kåfjord Nappe. Jettan consists of garnet–quartz–mica schists with amphibole-rich layers in the lower parts and alternating layers of calc-silicate gneiss and calcite marble in the uppermost parts (Zwaan et al., 2006; Skrede, 2013). Gámanjunni comprises mica schists dominated by biotite relative to muscovite and includes amphibole-rich layers and lenses (Böhme et al., 2016b; Quenardel and Zwaan, 2008). Lithological heterogeneity at Jettan introduces multiple potential weakness zones, whereas Gámanjunni's more homogeneous mica schist favors the development of a single dominant shear zone. Gámanjunni moves as a fractured but coherent rock mass along a fault plane (Böhme et al., 2016b), contrasting with the compartmentalized blocks of the Jettan landslide (Blikra et al., 2015) (see Figures 2 and 3). A coherent displacement pattern suggests a more mature landsliding system (Handwerger et al., 2016; Kristensen et al., 2021), evident from displacement vectors following the fall line of Gámanjunni's failure surface at the backscarp, where the block is displaced by 150 m (Böhme et al., 2016b). Comparatively, Jettan's failure surface appears less developed and dips more steeply than displacement vectors, with little vertical offset (Figures 2, 4). At Jettan, foliation dips in the same direction as the slope, but at a gentler angle, intersecting the surface downslope. In contrast, Gámanjunni's inward-dipping foliation does not intersect the surface down-slope, implying that outcropping requires a lower-angle sliding surface, likely involving internal deformation or shearing within the rock mass, as indicated by the bulging toe.

Permafrost at the Gámanjunni landslide may contribute to temperature-dependent creep (Krautblatter et al., 2013; Mamot et al., 2018). A long-term relationship has been observed between increasing landslide velocity and rising mean annual rock surface temperature as permafrost thaws (Penna et al., 2023a; Böhme et al., 2019; Hilger et al., 2021). Permafrost is likely absent at Jettan, eliminating this mechanism. A combination of a well-developed shear plane, coherent rock mass movement, and thawing permafrost inside the landslide could be the key factors driving Gámanjunni's faster displacement.

https://doi.org/10.5194/egusphere-2026-62
Preprint. Discussion started: 22 January 2026

We interpret that the earlier onset of annual warming at Jettan, due to its lower altitude, leads to earlier snowmelt and infiltration, initiating slip acceleration 17 days before Gámanjunni in average (Figure 5). This observation highlights that landslides influenced by permafrost and those without permafrost can accelerate at similar times yet exhibit different velocities. Importantly, higher velocities do not necessarily indicate greater hazard. At Gámanjunni, increased velocity may result from temperature-dependent creep, which is unlikely to cause catastrophic failure given the pressure and temperature conditions at the shear-plane depth. In northern Norway, rock slope failures are considerably less frequent than in southern Norway (Penna et al., 2023b). This contrast between active landslides and the absence of historic large-scale slope failures may reflect the stabilizing influence of permafrost or the mechanical properties of mica-rich bedrock, both of which can inhibit rapid failure (Penna et al., 2023a). These same factors may also promote the persistence of active landslides. Although both landslides exhibit comparable surface kinematics, only Jettan has detailed subsurface data, enabling deeper investigation of its seasonal dynamics in the following sections.

4.2 Volumetric Versus Localized Deformation at Jettan Landslide

Subsurface borehole data from the Jettan landslide provide insight into its deformation characteristics. Borehole instruments record displacement along their entire depth, whereas GNSS measures cumulative surface displacement of the whole landslide body. The similar total displacement observed between the two datasets indicates that the boreholes capture the majority of landslide movement.

Borehole data reveal that most displacement occurs within the rock volume rather than along a discrete shear zone, as shown by cumulative displacement profiles in Figure 4. The Jettan landslide comprises both mica-rich rocks, which are known to exhibit slow creeping behavior (Penna et al., 2023a; Böhme et al., 2013), and alternating layers of gneiss and calcite. This deformation may be facilitated by multiple planes of weakness within the rock mass (Elvebakk, 2013, 2014), enabling distributed strain along structurally weakened pathways (Eberhardt et al., 2004; Rechberger et al., 2021).

Comparable volumetric displacement has been documented at the Åknes landslide in borehole KH-02-06 (Aspaas et al., 2024), which uses the same instrumentation as Jettan. However, newer boreholes at Åknes do not exhibit similar patterns, suggesting that instrument-specific limitations or installation conditions may influence the observed deformation.

4.3 Evolution of Localized Deformation

After characterizing the overall volumetric deformation, we now discuss the development and acceleration of the localized shear zone in borehole BH 1, which exhibits the most pronounced deformation (Figure 6). Borehole BH-2 upper shear zone and BH-3 are referenced for comparison, while the lower shear zone in BH-2 remains steady during this analysis and is not discussed further.

https://doi.org/10.5194/egusphere-2026-62
Preprint. Discussion started: 22 January 2026

Prior to the onset of shear-zone accelerations in 2020, 2022, and 2025, displacement in borehole BH-1 was predominantly accommodated within the rock mass. These acceleration phases lead to higher deformation rates and generally coincide with years of deeper snowpacks and more intense snowmelt, with the exception of 2021 (Figure 2). Although relocation of the Jettan weather station may introduce uncertainty in long-term trends, comparison with the Lyngseidet station shows similar maximum snow depth patterns (Figure A4), supporting the observed correlation between snow depth and displacement rates. Displacement in borehole BH-1 also correlates moderately with the 14-day running sum of rain and snowmelt, with a 23-day lag, indicating that water infiltration is a key driver. This extended lag may reflect prolonged saturation, possibly linked to shear-plane depth or multi-year ice in the back scarp. Comparable relationships between groundwater pressure and landslide velocity have been documented in other slow-moving landslides (Agliardi et al., 2020; Aspaas et al., 2024; Kristensen et al., 2021; Finnegan et al., 2022). However, because open boreholes can misrepresent subsurface water flow (Aspaas et al., 2024), hydromechanical effects of pore pressure and seepage forces are not addressed further.

Initial displacement behavior in borehole BH-1 (Figure 6) differs from the expected seasonal acceleration pattern. The absence of acceleration phases in the years before 2020 indicates that meteorological forcing alone cannot explain the three acceleration periods. A plausible explanation is structural modification within the shear zone, driven by progressive damage (Eberhardt et al., 2004). ARDL modeling supports this interpretation by identifying the dominant role of endogenous factors in controlling displacement. These findings suggest that internal processes increasingly govern deformation, which is consistent with a maturing and structurally evolving shear zone. This evolution may also explain the increased sensitivity to water infiltration observed in later years. Further evidence emerged after the spring acceleration of 2025, when BH-1 displayed a seasonal acceleration pattern similar to the upper zone in BH-2, characterized by rapid acceleration followed by deceleration.

A notable pattern appears when comparing boreholes BH-1 and BH-3, which are aligned along the landslide slope. Both initially show similar displacement rates, followed by acceleration in 2020. BH-3 then decelerated while BH-1 maintained high velocity. This difference may reflect transient loading associated with strain accumulation and horizontal stress redistribution (Leshchinsky et al., 2019; Lacroix et al., 2020), culminating in a burst of acceleration in BH-3, before slowing. A similar imbalance recurs in 2025, as BH-3 accelerates following an earlier acceleration in BH-1 (Figure 6). The relationship between these two boreholes is also supported by the ARDL model. Comparable patterns of transient acceleration and strain redistribution have been documented at the Åknes landslide (Aspaas et al., 2024).

The Jettan landslide comprises several individual blocks that exhibit different deformation patterns and hydrological sensitivities. At times, boreholes BH-1 and BH-3 appear mechanically coupled, while at other times they behave independently due to diverging velocities. We infer that the boreholes sample local asperities within a potential plane that is yet to coalesce into one through-going shear zone, where progressive damage modifies mechanical parameters locally, whereas strain imbalances act at a larger scale to influence the overall evolution of the shear

https://doi.org/10.5194/egusphere-2026-62
Preprint. Discussion started: 22 January 2026

zone. The increasing occurrence of simultaneous slip across these asperities suggests a maturing failure surface with an increasing likelihood of catastrophic collapse.

4.4 Rheological Evolution of the Jettan Landslide

Ambient seismic noise analysis reveals a clear cyclical seasonal pattern in apparent seismic velocity changes (dv/v) (Figure 7). Seismic velocity reductions typically begin in mid-spring and persist until early winter, with two distinct minima in summer and autumn. Because ambient noise is sensitive to changes within the landslide volume, these variations likely reflect changes in water content, temperature, or mechanical rigidity (Larose et al., 2015).

Cross-correlation analysis shows strong negative relationships between dv/v and shallow ground temperature (1 m depth), the 14-day sum of rain and snowmelt, and borehole BH-1 velocity. The long-term cyclicity of dv/v suggests a similarly fluctuating controlling mechanism. From 2013 to 2020, borehole BH-1 displacement exhibited a predominantly linear, non-seasonal trend, indicating that dv/v does not directly reflect shear zone stability. While both shallow temperature and water availability display seasonal signals, only rain and snowmelt exhibit two distinct annual peaks. Previous studies have shown that dv/v decreases with wetting and increases with drying of the medium (Liu et al., 2024; Borgeat et al., 2025). The first drop in dv/v coincides with peak velocities in GNSS and borehole shear zones, whereas the second drop aligns with GNSS acceleration but not with borehole acceleration. This pattern suggests that spring acceleration reflects localized shear deformation, while autumn acceleration represents volumetric deformation of the landslide body. Collectively, these observations support an interpretation of an annual rheological transition from rigid to compliant behavior driven by progressive wetting of the landslide.

From a monitoring perspective, decreases in dv/v have been observed in other landslides prior to collapse (Mainsant et al., 2012) or acceleration (Liu et al., 2024), although such signals are not consistently observed across landslide sites (Borgeat et al., 2025). At Jettan, comparable drops in dv/v precede acceleration events, but thresholds proposed in previous studies, such as a two percent change before failure (Mainsant et al., 2012) or values exceeding two standard deviations, do not appear to serve as reliable precursors to catastrophic failure in this case.

A gradual negative trend in dv/v is observed since 2019. Linear regression indicates a consistent rate of approximately -0.23% per year. This trend may reflect progressive internal changes within the landslide system, such as increased water content or reduced structural integrity, which could facilitate future failure. However, this trend applies only to the observed period and should not be extrapolated, as future environmental or mechanical conditions may alter system behavior.

The seasonal signal in dv/v provides a valuable proxy for tracking water infiltration within the landslide body. These observations offer a physical explanation for the annual kinematic behavior of the landslide, where water saturation drives a transition from rigid block-like movement to compliant volumetric deformation. This rheological shift highlights the role of hydrological forcing in modulating landslide dynamics on a seasonal basis.

https://doi.org/10.5194/egusphere-2026-62
Preprint. Discussion started: 22 January 2026

5 Conclusions

An increasing number of landslide failures have been reported across both Arctic and high-altitude regions (Pei et al., 2023; Penna et al., 2023a), areas characterized by widespread permafrost and amplified warming driven by climate change (Rantanen et al., 2022). Many of these landslides exhibit creep rates from one to more than ten centimeters per year, and statistically significant links have been established between permafrost warming and accelerated landslide motion (Penna et al., 2023a). Yet, the physical processes governing Arctic landslide behavior remain poorly understood.

This study compares two Arctic landslides in northern Norway, Gámanjunni and Jettan, separated by only 10 km. At Gámanjunni, geophysical observations indicate the presence of permafrost, whereas Jettan appears to lack it. Despite this difference, both landslides exhibit similar seasonal kinematics, although Gámanjunni creeps roughly three times faster. The mica-rich lithology and possible permafrost conditions may help explain the region's high proportion of active landslides. Subsurface data from Jettan reveal that deformation is controlled by both endogenous and exogenous factors. Local asperities within shear zones likely undergo progressive damage, increasing sensitivity to water infiltration, while strain imbalances across the landslide body drive large-scale shear zone evolution. Apparent seismic velocity changes in the landslide volume further indicate a seasonal transition from localized to volumetric deformation modulated by hydrological forcing.

These findings provide new insights into the internal dynamics of Arctic landslides. Water infiltration emerges as the dominant factor controlling seasonal acceleration, while permafrost, if present, appears to influence long-term creep rates. By integrating subsurface observations with surface kinematics, this study strengthens the physical basis of Arctic landslide behavior and supports improved hazard assessments and monitoring strategies in rapidly warming polar regions.

Code and data availability. The timeseries data used for the analysis of the two landslides in the study are available at Aspaas and Renard (2026), hosted and preserved on NIRD under a Creative Commons open data license. The JupyterLab Notebook used to perform the analysis presented in the paper is available at Aspaas (2025), hosted on GitHub and archived on Zenodo.

Appendix A

A1 describes the seismic data analysis, supported by Figures A2, and A5–A11, and Tables A6–A7. A2 provides details of simulated ground temperatures at the location of borehole BH-1 in the Jettan landslide, with Figure A4 comparing observed and modeled temperatures. Figure A1 validates rolling functions and cross-correlation without introducing artificial lags, while Figure A3 presents the comparison between the Lyngseidet meteorological station and the seNorge dataset for Jettan. Tables A1–A3 summarize instrumentation at the two landslides and provide additional information on borehole depth and shear zone composition. Tables A4 and A5 summarize the Auto

https://doi.org/10.5194/egusphere-2026-62
Preprint. Discussion started: 22 January 2026

Regressive Distributed Lags (ARDL) models' results. Monitoring of the Jettan and Gámanjunni landslides has been continuous since instrument installation, with all data recorded and stored by the Norwegian Water Resources and Energy Directorate. These datasets were retrieved and processed as described in the Methods section of the main manuscript. Ground temperature modeling data were obtained from the Norwegian Meteorological Institute (A2).

A1

This section presents how seismic data were processed to obtain the time series of the variation of the apparent velocity of surface waves (dv/v). This is achieved in two main steps: 1) evaluation of the sensitivity of surface waves as a function of frequency and depth and 2) computation of dv/v from raw seismic data.

The first step consists of defining a one-dimensional synthetic seismic stratification model. This stage is compulsory to define the frequency range to retain to compute the dv/v time series in the desired depth range. To evaluate this sensitivity, several geomechanical parameters are required for each subsurface unit, namely their thickness, P- and S-wave velocity (V_P and V_S, respectively) and unit weight (ρ).

Thickness and V_P were retrieved from previous reports: a morphological cross-section (Blikra and Christiansen, 2014) and a seismic refraction profile (Rønning et al., 2008). The location of these profiles is shown in Figure A6 and they are presented in Figures A7 and A8, respectively.

The vertical distribution of V_S was determined using two approaches. First, the empirical relationship of Brocher (2005a) was tested. It relates V_P and V_S (both in km/s) to a variety of crustal materials and reads:

$$V_S = 0.7858 - 1.2344V_P + 0.7949V_P^2 - 0.1238V_P^3 + 0.0064V_P^4. \quad \text{(A1)}$$

The values obtained are consistent with the geomechanical units in place, with the exception of the strongly fractured rock unit, which provided a too low velocity (285 m/s). To circumvent this issue, another approach was tested: since all parameters were established, the only remaining unknown is V_S in this unit. Then, it was calculated using a trial and error method using the analytical formula proposed by Dobry et al. (1976). This formula allows for the determination of the resonance frequency f_0 of a subsurface profile using only the thickness and V_S of its different units. The resonance frequency was experimentally determined from measurements of seismic ambient noise at the JETT station and the results are shown in Figure A9. Approximately 79 000 hourly seismograms between 2016 and 2024 were used to compute the Horizontal-to-Vertical (H/V) ratio with the geopsy package (Wathelet et al., 2020). The black curve in Figure A9 represents the most probable H/V curve, with a maximum (but moderate) amplification of around 3 at $f_{H/V} = 2.5$ Hz. Assuming that the measured $f_{H/V}$ corresponds to the resonance frequency of the first 60 m below ground (10 m of landslide mass plus 50 m of strongly fractured rock; A6), V_S in the unit "strongly fractured rock" was adjusted to obtain $f_0 = f_{H/V} = 2.5$ Hz. This led to $V_S = 750$ m/s, which is consistent with the other geomechanical parameters of this unit. Finally, unit weight was taken as the median of the measurements obtained by Vick et al. (2021), which are shown in Table A6.

https://doi.org/10.5194/egusphere-2026-62
Preprint. Discussion started: 22 January 2026

The final 1D geomechanical model in the vicinity of seismic station JETT is presented in Table A7. It was used to compute the sensitivity kernels of surface waves, *i.e.* their sensitivity as a function of frequency and depth. The computation was conducted using Disba (Luu, 2021), which is a Python package that implements a subset of codes from the Computer Programs in Seismology (Herrmann, 2013). The results are shown in Figure A10. Figure A10a resumes the 1D synthetic model established previously and Figure A10b shows the dispersion curves of the fundamental mode of Rayleigh and Love waves corresponding to the synthetic model. Figures A10c and A10d show the sensitivity kernels of Rayleigh and Love waves, respectively.

Raw seismograms were processed as described in the main text and the present section aims at providing supporting, but non essential information. The daily correlograms for pair of components Vertical-East (Z-E), bandpass-filtered in the range [4.5-6.5] Hz are shown in Figure A11. The subplot on the right shows the SVD-Wiener-filtered correlograms. The vertical dashed lines represent the limits of the lag time that was used to compute *dv/v*, between [-2:-0.2] and [0.2:2] s, and the reference correlogram is represented as a red curve. This time range allows us to get rid of potential autocorrelation near zero lag and focus on scattered surface waves.

Individual *dv/v* time series are presented in Figure A12. Briefly, curves showing the highest amplitude of variation in both *dv/v* and *cc* are those which encompass the East-West component. This is because it is the main degree of freedom of the landslide mass. The curve at the bottom of the figure corresponds to the average of the three components, weighed by their individual *cc*, and is the curve used in the paper. This approach has been proposed by Hobiger et al. (2014) and the weighed average *dv/v* is obtained using:

$$dv/v(t) = \frac{\sum_{k=1}^{N} CC_k^2(t) \cdot dv/v_k(t)}{CC_k^2(t) \cdot dv/v_k(t)}, \tag{A2}$$

where k is the pair of components, N is the total number of pairs of components (three in this work), CC is the weigh-averaged coefficient of correlation. CC is obtained using:

$$CC(t) = \frac{\sum_{k=1}^{N} CC_k^2(t)}{\sum_{k=1}^{N} CC_k^3(t)}. \tag{A3}$$

Finally, Figure A3 shows the complete *dv/v* time series from January 2016 to July 2025.

A2

We applied the CryoGrid community model (Westermann et al., 2023) to simulate ground temperature along a vertical profile at borehole BH-1 of the Jettan landslide to fill gaps in the observational data. We modeled a 1D column from the ground surface to a depth of 130 m, considering altitude and slope angle, provided by the Digital Elevation Model at the borehole location.

https://doi.org/10.5194/egusphere-2026-62
Preprint. Discussion started: 22 January 2026

We used a time series of NORA3 (Haakenstad et al., 2021; Haakenstad and Breivik, 2022)[data retrieved from The Norwegian Meteorological Institute] as forcing data, spanning from 1965 to 2023 with a 3 km resolution. The data were downscaled following the topoSCALE routine implemented in CryoGrid (Fiddes and Gruber, 2014), and bias-corrected for air temperature using a day-of-year quantile mapping approach (Themeßl et al., 2012) with in-situ observations from the meteorological station at Jettan (Figure 2, main text). To extend the time series back to 1850, monthly mean anomalies from CESM2 (Danabasoglu et al., 2020) were applied to the NORA3 data. The simulations covered the time period from 1850 to 2023, with the first 10 years serving for the accelerated spin-up (Westermann et al., 2023). Only the time period from 01.09.2019 to 01.09.2023 was used for further analysis.

The model domain was defined by two stratigraphy classes, each with specific physics describing the thermal state and water/ice balance. In the upper five meters, the stratigraphy class GROUND-freezeC-bucketW-seb was used to calculate the surface energy balance, soil freezing characteristics after (Painter and Karra, 2014), and the water balance based on a bucket scheme, meaning that soil water is retained within the soil matrix, or it moves downwards due to gravitational forces (Westermann et al., 2023). Removal of surface water was based on the Gauckler-Manning equation. Below five meters depth, we applied the stratigraphy class GROUND-freeW-seb, which simplified the freezing characteristics to a phase change of water at 0 ° C, and water and ice contents to a constant sum. The surface albedo was set to 0.15, and the surface roughness to 0.01 m. With bedrock characterizing the soil profile, a porosity between 5% and 7.5%, and a field capacity of 0.03 were specified.

Seasonal snow was represented by the Crocus-based snow class (Vionnet et al., 2012), considering wind compaction, initial snow density, and varying surface albedo. A snowfall factor multiplied with the forcing data allowed for the representation of local differences in snow accumulation.

To address uncertainties in rock characteristics and snow accumulation, we ran the model with 12 varying parameter sets: porosity of 5% or 7.5%, thermal conductivity of 2.8 W/mK or 3.0 W/mK, and snowfall factors of 1, 1.1, or 1.2. The median value across all scenarios was taken for analysis. The model results were validated against observational data from borehole BH-1 and showed good agreement at different depths. In the year 2023, at 115 m depth, a ground temperature of 2.20 ° C was measured, while the model simulated 2.23 ° C. At 45 m depth, the measured temperature was 1.86° C, compared to the simulation result of 1.72 ° C. At the ground surface (Figure A5), the simulation could capture the seasonal temperature signal, particularly during snow-free conditions, when movements in the landslide occur. Larger discrepancies were observed during the snow season, which can be traced back to a poor representation of individual snowfall events and snow redistribution in the complex terrain of Jettan, which goes beyond the model's capacities.

https://doi.org/10.5194/egusphere-2026-62
Preprint. Discussion started: 22 January 2026

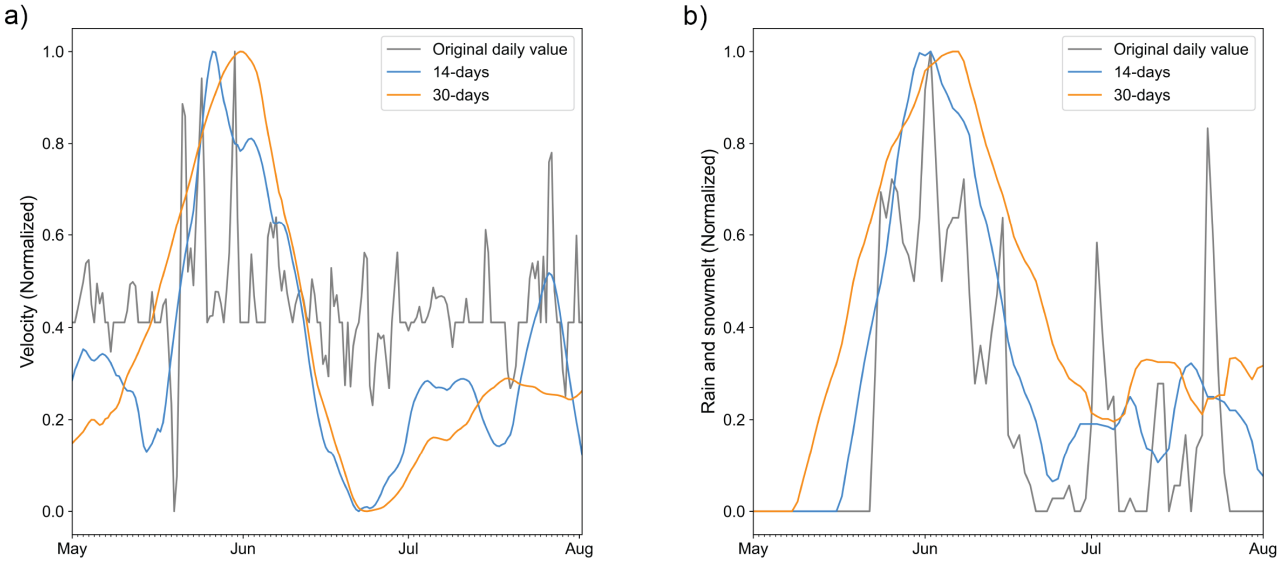

Figure A1. Verification of zero lag created by the window lengths by the rolling functions. a) Normalized velocity from GPS-4 on Jettan with 1-day, 14-days, and 30-days velocity calculated by the centered rolling linear regression function (see Section Integration of Data). b) Normalized rain and snowmelt summed over 1-day, 14-days, and 30-days by the centered running sum function.

https://doi.org/10.5194/egusphere-2026-62
Preprint. Discussion started: 22 January 2026

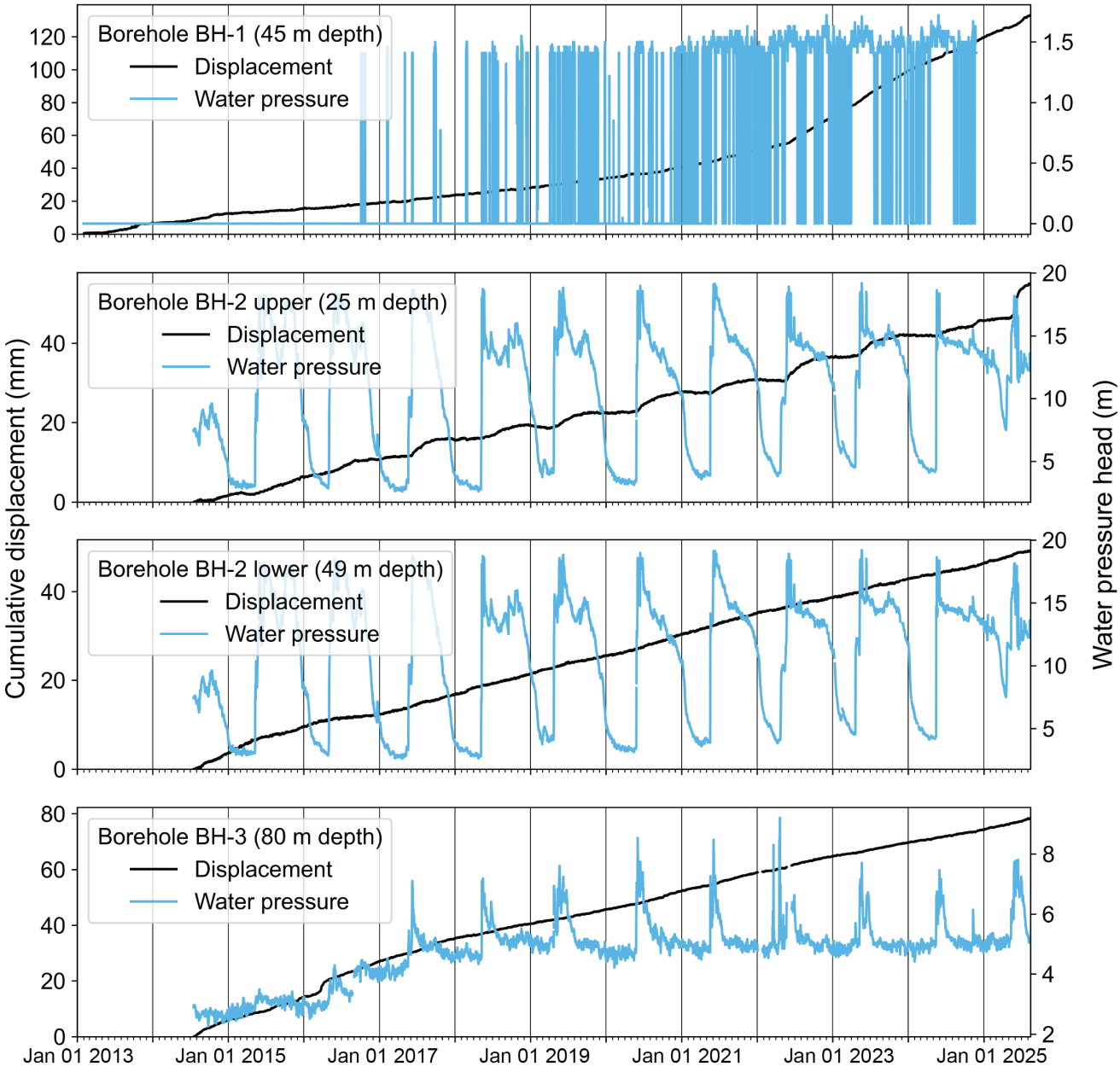

Figure A2. Time series of cumulative displacement (black) and water pressure head (blue) in the Jettan landslide. Data are measured in the shear zone inclinometers of borehole BH-1 (a), the two shear zones of borehole BH-2 (b and c), and the shear zone of borehole BH-3 (d) are presented. The water pressure in each borehole is equivalent to the meters of water column height above the sensor measured at approximately 100 meters depth in open boreholes.

https://doi.org/10.5194/egusphere-2026-62
Preprint. Discussion started: 22 January 2026

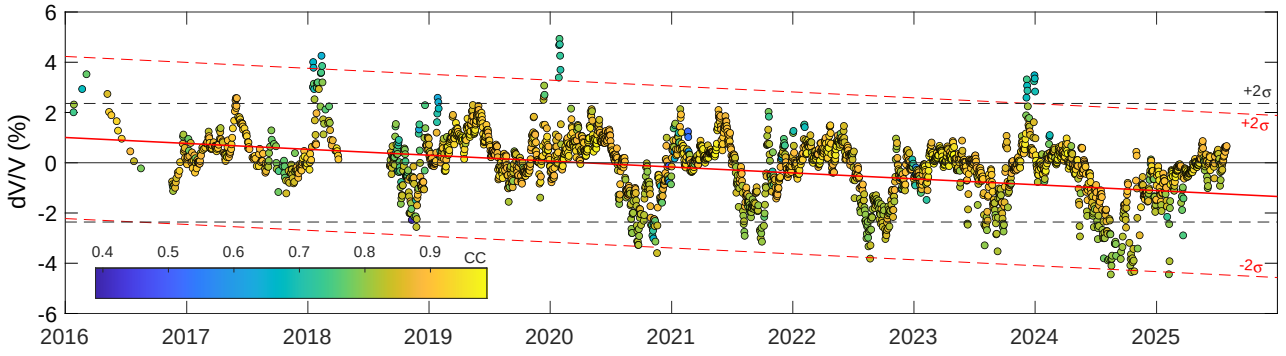

Figure A3. Daily dv/v time series (not smoothed) computed between 4.5 and 6.5 Hz, which corresponds to the time series presented in the main text. The color scale refers to the coefficient of correlation between the reference and each daily correlograms. Horizontal dashed lines stand for the 95% confidence interval between -2 and 2σ (with $\sigma = \pm 1.18\%$). The red line represents the linear trend of the time series with an annual decrease of 0.23%, and the red dashed lines the corresponding 95% confidence interval (with $\sigma = \pm 1.6\%$).

https://doi.org/10.5194/egusphere-2026-62
Preprint. Discussion started: 22 January 2026

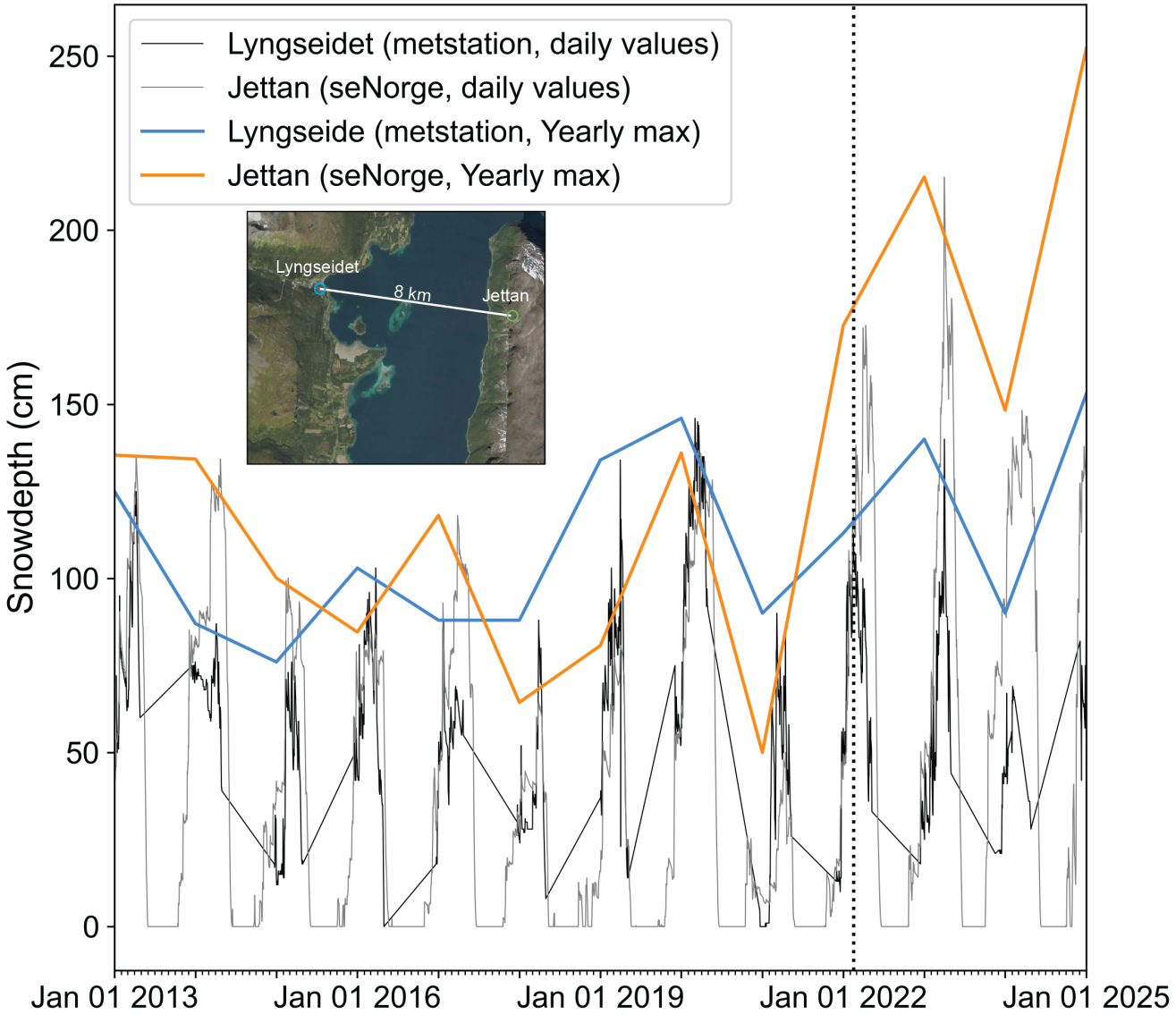

Figure A4. Daily snow depth values from the Lyngseide meteorological station across the fjord from Jettan and the seNorge modeled dataset. More snow could be accumulating on the new station as we see an increase after 2022 in the seNorge dataset and no such increase at the Lyngseide station.

https://doi.org/10.5194/egusphere-2026-62
Preprint. Discussion started: 22 January 2026

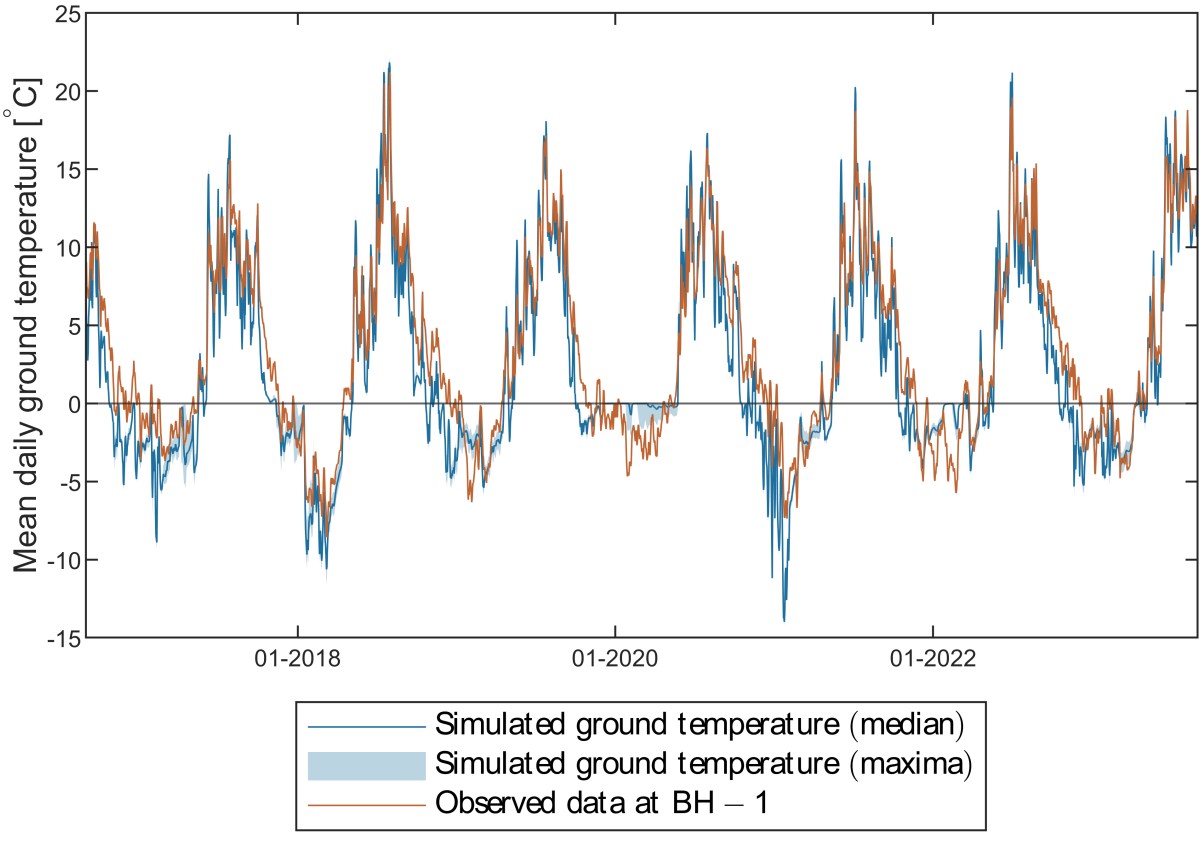

Figure A5. Simulated and observed ground temperatures at one meter depth in borehole BH-1 in the Jettan landslide. The simulations include 12 varying parameter sets to account for uncertainties in the bedrock characteristics and snow dynamics. The model setup is described in A2.

https://doi.org/10.5194/egusphere-2026-62
Preprint. Discussion started: 22 January 2026

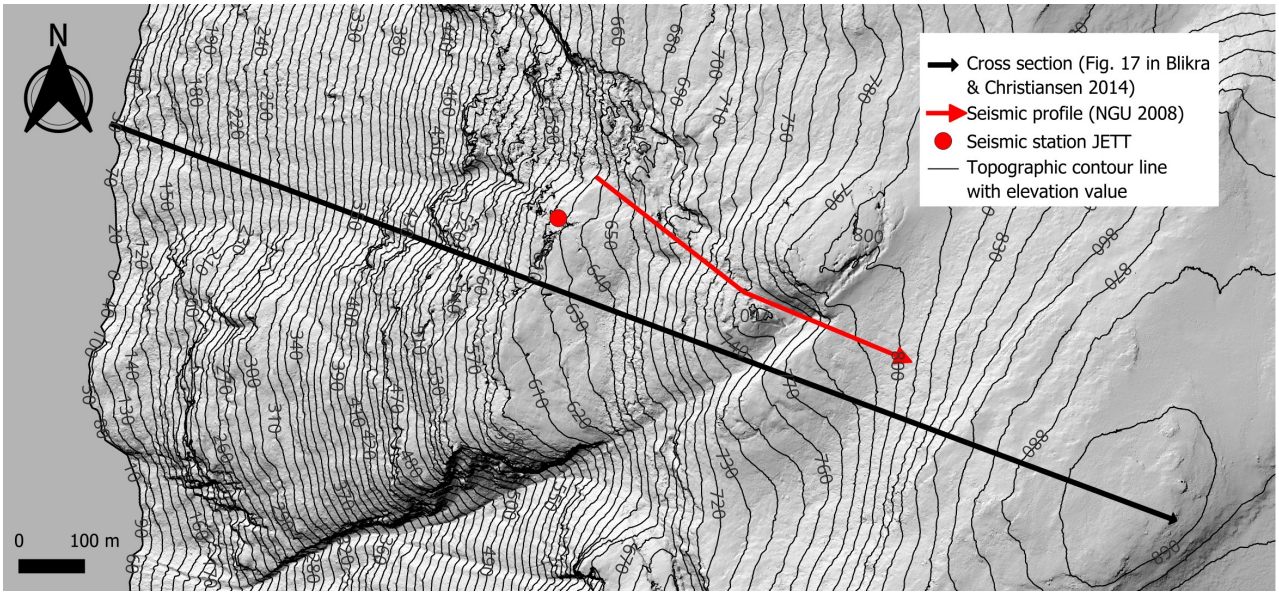

Figure A6. Location of the seismic measurements. The black arrow represents the cross-section presented in Figure A7.

https://doi.org/10.5194/egusphere-2026-62
Preprint. Discussion started: 22 January 2026

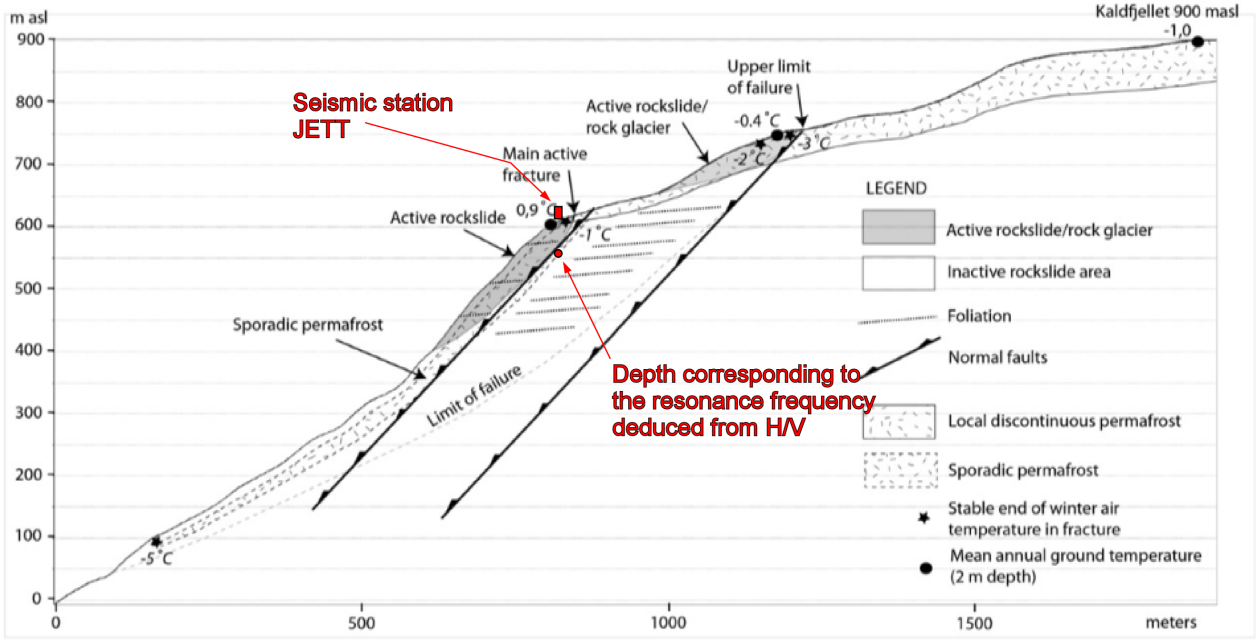

Figure A7. Profile of the Jettan rockslide, modified from Blikra and Christiansen (2014).

https://doi.org/10.5194/egusphere-2026-62
Preprint. Discussion started: 22 January 2026

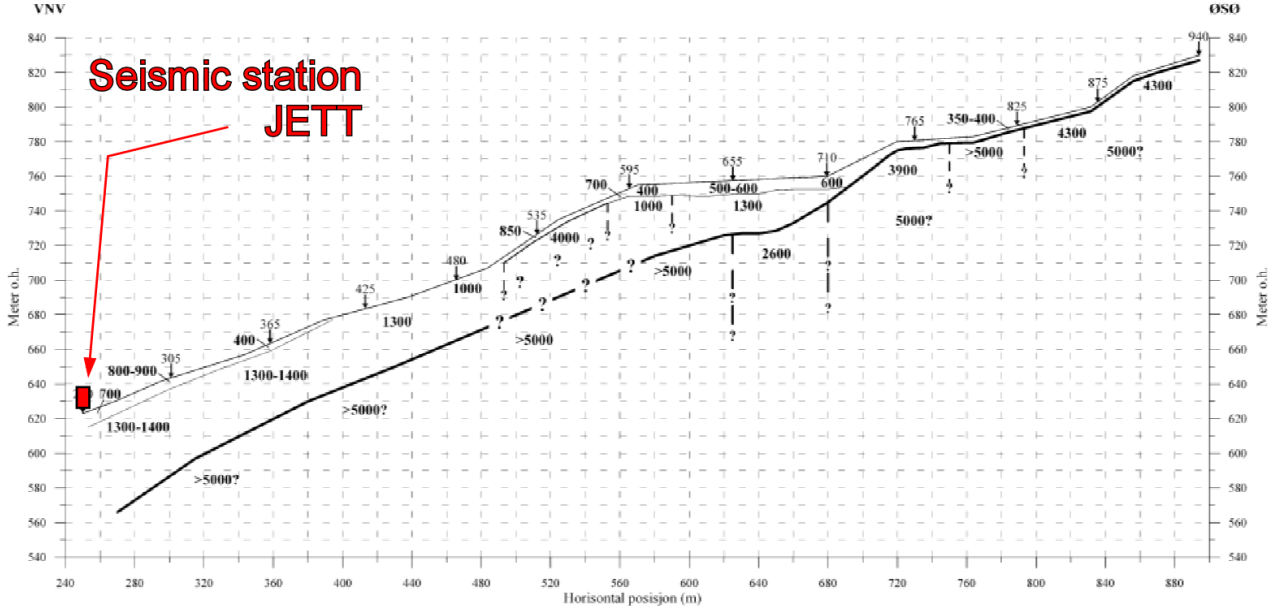

Figure A8. Seismic refraction profile in the upper part of the Jettan rockslide (Rønning et al., 2008). The location of the profile is shown in Figure A7.

https://doi.org/10.5194/egusphere-2026-62
Preprint. Discussion started: 22 January 2026

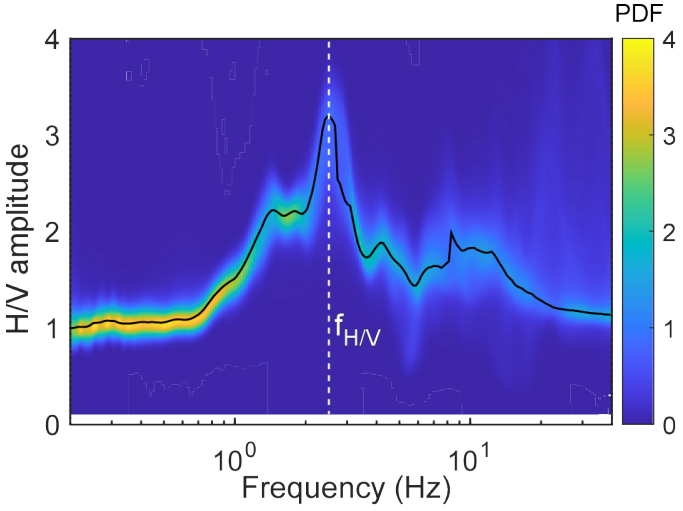

Figure A9. The average H/V curve at seismic station JETT. The probability density function (PDF) was established using around 79 000 hourly curves between 2016 and 2024. The black curve represents the maximum PDF. The white dashed line shows a maximum (but moderate) amplification of around 3 at frequency $f_{H/V} = 3.5$ Hz.

https://doi.org/10.5194/egusphere-2026-62
Preprint. Discussion started: 22 January 2026

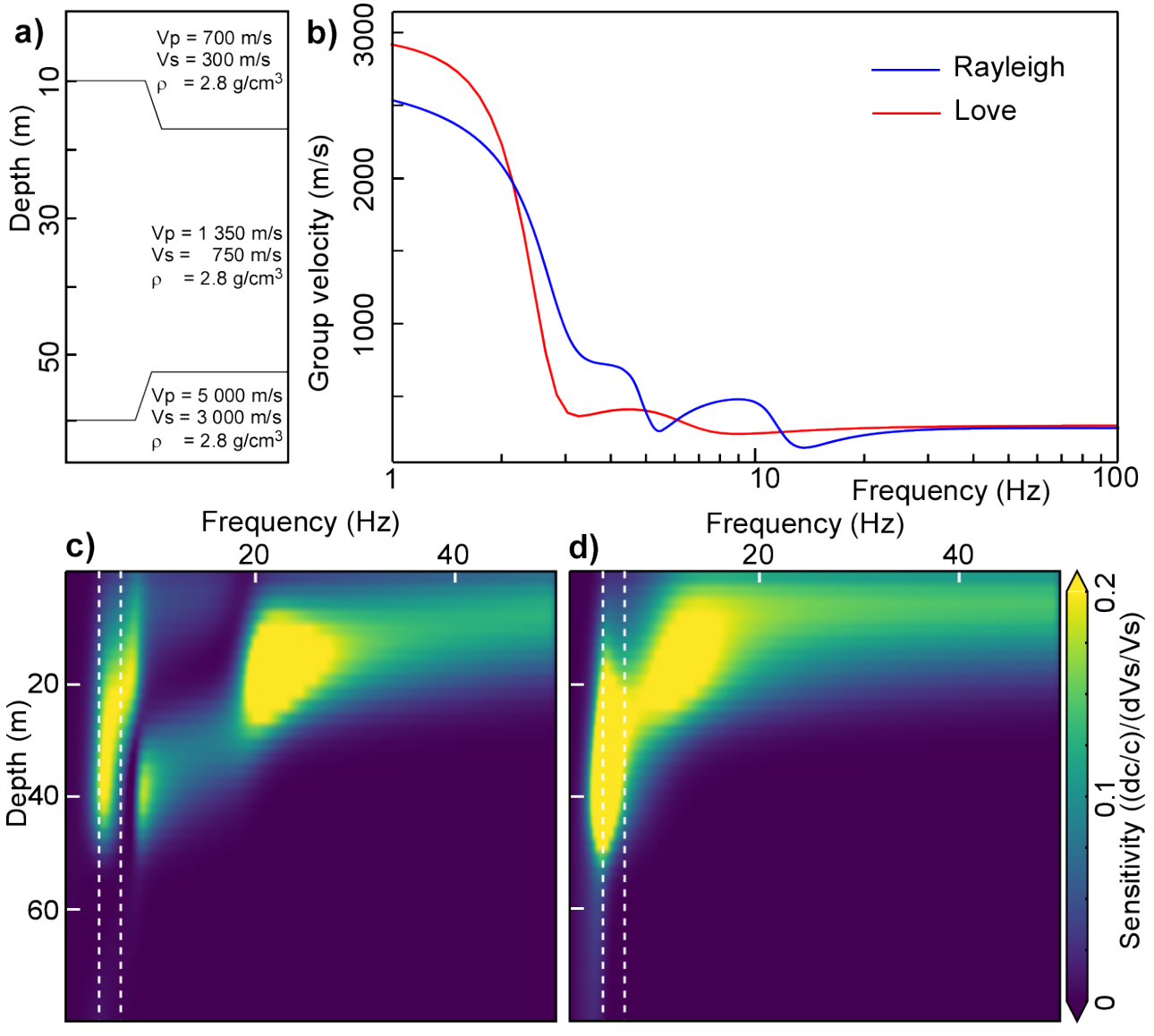

Figure A10. Sensitivity kernels of surface waves at the Jettan rockslide. a) Seismic stratification. b) Theoretical dispersion curves of the fundamental modes of Rayleigh and Love waves. c) and d) Sensitivity of Rayleigh and Love waves, respectively, as a function of depth and frequency. The white dashed lines represent the frequency range (4.5-6.5 Hz) used in the paper.

https://doi.org/10.5194/egusphere-2026-62
Preprint. Discussion started: 22 January 2026

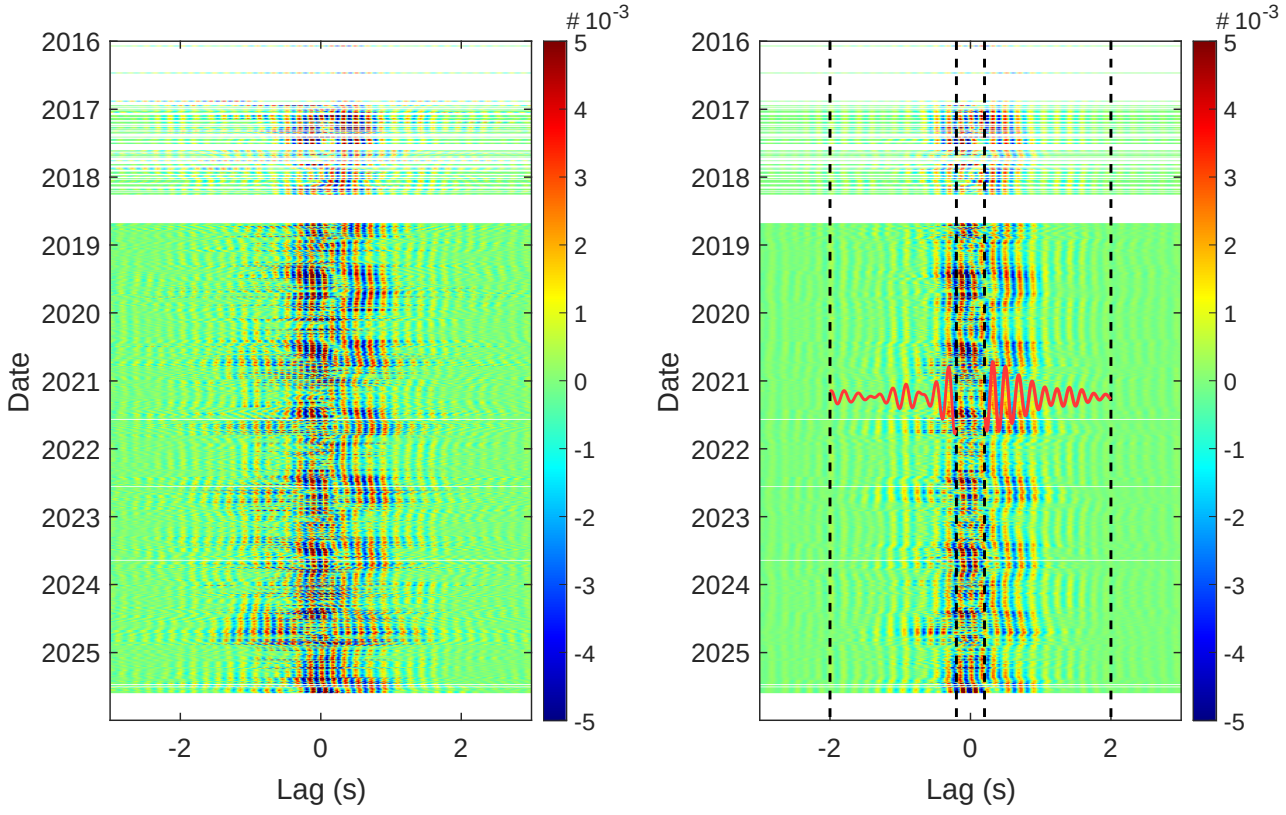

Figure A11. Daily correlograms at Jettan between vertical and east-west components, and filtered between 4.5 and 6.5 Hz. **Left**: raw correlograms. **Right**: Correlograms after the Wiener-SVD filtering (Moreau et al., 2017). The vertical dashed lines represent the time range ([-2:-0.2]s and [0.2:2]s) used for computing the dv/v time series.

https://doi.org/10.5194/egusphere-2026-62
Preprint. Discussion started: 22 January 2026

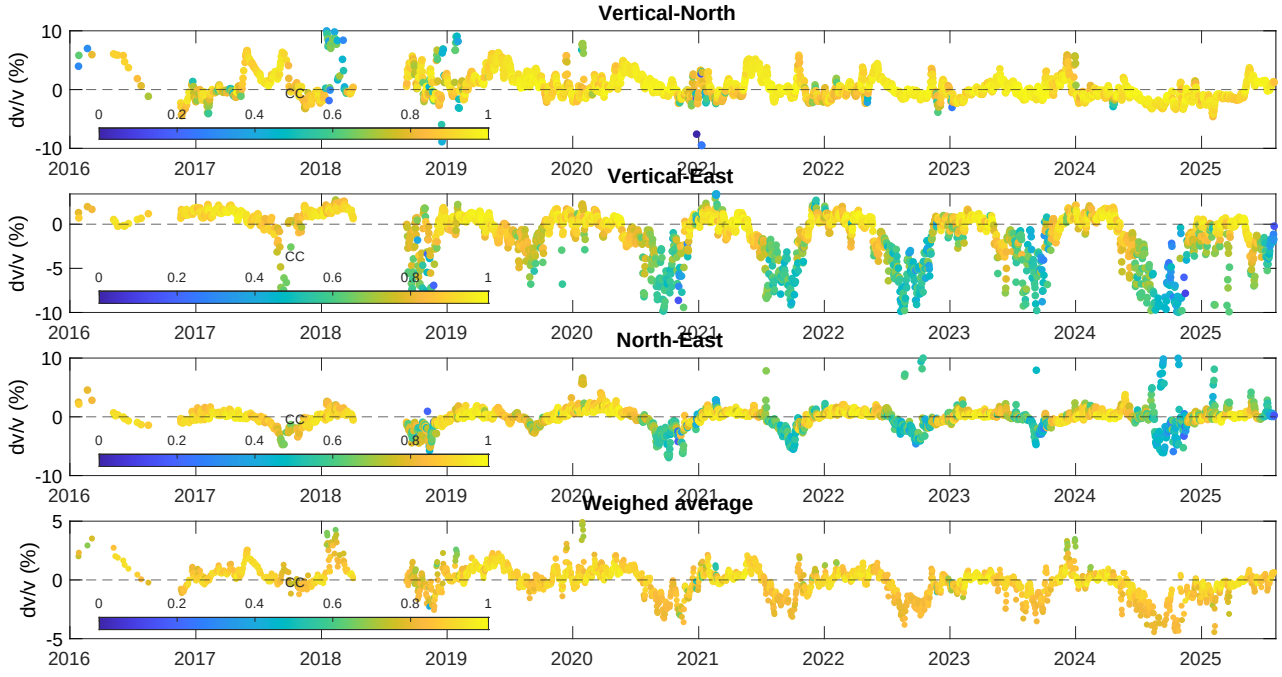

Figure A12. Time series of dv/v at seismic station JETT. The first three graphs show individual time series for the three possible pairs of components Vertical-North (Z-N), Vertical-East (Z-E) and North-East (N-E). The graph at the bottom shows the average dv/v time series where each dv/v value is weighed by its coefficient of correlation.

https://doi.org/10.5194/egusphere-2026-62
Preprint. Discussion started: 22 January 2026

Table A1. Table of instruments installed on the Jettan landslide by type, product name, number of devices, installation date, analyzed period, acquisition frequency, and measurement resolution provided by the manufacturer.

Type	Product name	Number of instruments	Installation date(s)	Analyzed period	Sampling frequency	Measurement resolution
GNSS	Trimble Net-R9 receivers with Trimble Zephyr 2 or 3 antennas	10	19.02.2010-16.07.2010	∼10 years	1 s	<1 mm
Borehole inclinometers						<0.3 mm
Borehole water pressure sensor	CSG DMS 2D Rock	3	01.03.2013-17.07.2014	∼12 years	1 hr	138 Pa
Temperature sensors						0.1 ° C
Seismometer	Guralp CMG-3E	1	05.11.2014	∼7 years	200 Hz	
Old meteorological station	Campbell SR50 - Snow depth	1	29.05.2014	∼7 years	1 hr	0.25 mm
	Vaisala HMP45A - Temperature	1				0.2 ° C
	Geonor T -200B - Precipitation	1				0.1 mm
New meteorological station	Lufft SHM31 - Snow depth	1	17.02.2022	∼3 years	1 hr	5 mm
	Vaisala HMP155 - Temperature	1				0.2 ° C
	Geonor T-200B - Precipitation	1				0.1 mm

https://doi.org/10.5194/egusphere-2026-62
Preprint. Discussion started: 22 January 2026

Table A2. Table of instruments installed on the Gámanjunni landslide by type, product name, number of devices, installation date, analyzed period, acquisition frequency, and measurement resolution provided by the manufacturer.

Type	Product name	Number of instruments	Installation date(s)	Analyzed period	Sampling frequency	Measurement resolution
GNSS	Trimble Net-R9 receivers with Trimble Zephyr 2 or 3 antennas	8	09.08.2015-10.02.2017	∼6 years	1 s	<1 mm
Meteorological station	Sommer USH-9 - Snow depth	1	10.12.2017	∼6 years	1 hr	1 mm
	Vaisala HMP155 - Temperature	1				0.2 ° C
	Geonor T -200B - Precipitation	1				0.1 mm

https://doi.org/10.5194/egusphere-2026-62
Preprint. Discussion started: 22 January 2026

Table A3. Table of boreholes installed at the Jettan landslide, displaying the detection period, shear plane depth, material composition of the shear zone, and the total instrument depth.

Borehole	Period		Shear plane	Depth (meters below ground)	Composition	Total depth of borehole instrument (m)
BH-1	01.03.2013	to		45-46	25 cm thick carbonate breccia mixed possibly with clay in the fault plane dipping 65-70° while the top of the fault zone dips ∼40° [a].	120
	27.11.2024					
BH-2	17.07.2014	to	Upper	25-26	Banded iron-rich garnet micaschist. Core loss and open fractures from 24-28 m depth.	96
	27.11.2024					
			Lower	49-50	Banded iron-rich garnet micaschist that is deformed from 37 to 53 meters depth with repeating zones of crushed rocks and clays. The thickest clay zone is 13 cm thick at ∼47 meters with a fracture dipping 45° [b]. The entire zone we record movement in is core loss.	
BH-3	17.07.2014	to		79-81	20 cm zone of finely crushed rock in mica-rich schist. No clay was observed[b].	99
	27.11.2024					

The shear plane column indicates boreholes that intersect both an upper and a lower shear plane, whereas boreholes with one shear plane are left blank. [a](Ganerød, 2013). [b](Ganerød, 2014)

https://doi.org/10.5194/egusphere-2026-62
Preprint. Discussion started: 22 January 2026

Table A4. Autoregressive Distributed Lag (ARDL) model (see Eq. 2 in the main text) results for the upper shear zone in borehole BH-2. The table lists endogenous and exogenous variables included in the model, with their lag order denoted as `variable_name.L`n. For each term, the estimated coefficient (α for autoregressive terms and β for distributed lag terms) is shown along with its statistical significance (p-value). Larger absolute coefficients indicate a stronger influence on the modeled sliding velocity. The variable names are: BH-2 (borehole BH-2), BH-2_WP (borehole BH-2 water pressure), Air_temp (air temperature from seNorge), Rain_Snow (total precipitation from rain and snowmelt from seNorge), and dv/v (relative seismic velocity change).

Variable	Coefficient	p-value
BH-2.L1	**0.36**	$\mathbf{1.0 \times 10^{-9}}$
BH-2.L2	**-0.18**	$\mathbf{1.7 \times 10^{-3}}$
BH-2.L3	**0.15**	$\mathbf{4.3 \times 10^{-3}}$
BH-2_WP.L0	**0.04**	$\mathbf{5.4 \times 10^{-4}}$
Air_temp.L0	**0.05**	$\mathbf{2.3 \times 10^{-4}}$
Rain_Snow.L0	**0.10**	$\mathbf{6.1 \times 10^{-12}}$
dv/v.L0	**0.06**	$\mathbf{9.8 \times 10^{-13}}$

https://doi.org/10.5194/egusphere-2026-62
Preprint. Discussion started: 22 January 2026

Table A5. ARDL model results (see Eq. 2 in the main text) for the shear zone in borehole BH-1. The table lists endogenous and exogenous variables included in the model, with lag order indicated as `variable_name.L`n. For each term, the estimated coefficient (α for autoregressive terms and β for distributed lag terms) is shown together with its p-value, reflecting statistical significance. Larger absolute coefficients suggest a stronger influence on sliding velocity within the model. Variable names: BH-1 (borehole BH-1) and BH-3 (borehole BH-3).

Variable	Coefficient	p-value
BH-1.L1	**0.56**	$\mathbf{1.8 \times 10^{-17}}$
BH-1.L2	**-0.18**	$\mathbf{1.0 \times 10^{-2}}$
BH-1.L3	**0.28**	$\mathbf{8.3 \times 10^{-5}}$
BH-1.L4	-0.02	0.70
BH-1.L5	-0.08	0.26
BH-1.L6	0.09	0.20
BH-1.L7	0.07	0.29
BH-1.L8	**0.18**	$\mathbf{3.1 \times 10^{-3}}$
BH-3.L0	**0.07**	$\mathbf{7.8 \times 10^{-3}}$

https://doi.org/10.5194/egusphere-2026-62
Preprint. Discussion started: 22 January 2026

Sample lithology	Density [g/cm^3]	E-modulus [GPa]	Poisson's ratio	UCS [MPa]
Garnet mica schist	3.0	29.6	0	146
Garnet mica schist	2.9	31.7	0.06	206
Garnet mica schist	3.0	42.9	0.07	107
Mica schist	2.7	40.3	0.1	240
Mica schist	2.7	36.5	0.09	197
Mica schist	2.7	39.2	0.07	228
Calcite marble	2.8	38.5	0.2	90
Calcite marble	2.8	51.6	0.23	88
Calcite marble	2.8			97
Calcite marble	2.7	53.4	0.21	107
Calcite marble	2.7			104

Table A6. Geomechanical parameters of the lithological units (Vick et al., 2021).

https://doi.org/10.5194/egusphere-2026-62
Preprint. Discussion started: 22 January 2026

Landslide unit	Thickness (m)	Vp (m/s)	Vs (m/s)	Density (g/cm^3)
Landslide mass	10	700	300	2.8
Strongly fractured rock	50	1350	750	2.8
Massive rock	∞	5000	3000	2.8

Table A7. Geomechanical and seismic model used for the computation of the sensitivity kernels. Terminology of the units after Rønning et al. (2008). *Vp*: P-wave velocity; *Vs*: S-wave velocity. Blue: evaluated from empirical relationships (see text for details). red: evaluated from a trial and error approach (see text for details).

Author contributions. AA initiated this study, coordinated the synthesis of the datasets, and analyzed the time series. He wrote the first drafts of the paper and designed most of the figures. GB performed the ambient noise analysis and provided a time series of the apparent seismic velocity change, along with figures for the appendix. JA performed the Cryogrid model and provided a time series of the ground temperature, IS and LK provided on-site knowledge and interpretation of the data, and NL, PL, BE, and FR provided interpretation of the data. All authors contributed actively to the final versions of the paper.

Competing interests. There are no competing interest among the authors of this paper

Acknowledgements. We thank Martin Iver Jacobsen for his guidance on statistical modeling and Martina Bohme for valuable discussions on landslide mechanics. We are also grateful to the geologists and technicians of the rockslide group at NVE for their insights and technical support related to landslide mechanics and instrumentation. Additionally, we acknowledge CSG s.r.l. and Mario Lovisolo for their assistance and discussions regarding borehole instrumentation.

https://doi.org/10.5194/egusphere-2026-62
Preprint. Discussion started: 22 January 2026

References

Agliardi, F., Scuderi, M. M., Fusi, N., and Collettini, C.: Slow-to-fast transition of giant creeping rockslides modulated by undrained loading in basal shear zones, Nature communications, 11, 1352, 2020.

Albaric, J., Kühn, D., Ohrnberger, M., Langet, N., Harris, D., Polom, U., Lecomte, I., and Hillers, G.: Seismic Monitoring of Permafrost in Svalbard, Arctic Norway, Seismological Research Letters, 92, 2891–2904, https://doi.org/10.1785/0220200470, 2021.

Allen, S. and Huggel, C.: Extremely warm temperatures as a potential cause of recent high mountain rockfall, Global and Planetary Change, 107, 59–69, 2013.

Andresen, A.: Caledonian terranes of northern Norway and their characteristics, Trabajos de geología, 17, 103–117, 1988.

Aspaas, A.: JupyterLab Notebooks: Loading, preprocessing, correlations, and figures (version 2), DataCite.https://doi.org/10.5281/zenodo.17968496, 2025.

Aspaas, A. and Renard, F. c.: Seasonal and Inter-Annual Evolution of the Deformation of Two Arctic Landslides, https://doi.org/10.11582/2026.ESP7OMHG, 2026.

Aspaas, A., Lacroix, P., Sena, C., Kristensen, L., Langet, N., and Renard, F.: Creep bursts on the Åknes landslide, Norway: Detection, characterization and possible mechanisms, Journal of Geophysical Research: Earth Surface, 129, e2024JF007 733, 2024.

Ben-Yehoshua, D., Sæmundsson, Þ., Helgason, J. K., Belart, J. M., Sigurðsson, J. V., and Erlingsson, S.: Paraglacial exposure and collapse of glacial sediment: The 2013 landslide onto Svínafellsjökull, southeast Iceland, Earth Surface Processes and Landforms, 47, 2612–2627, 2022.

Bismans, F. J.: Specification of the ARDL Model, in: Dynamic Econometrics : Models and Applications, pp. 169–196, Springer Nature Switzerland : Imprint: Palgrave Macmillan, 2025.

Blikra, L. H. and Christiansen, H. H.: A field-based model of permafrost-controlled rockslide deformation in northern Norway, Geomorphology, 208, 34–49, 2014.

Blikra, L. H., Christiansen, H. H., Kristensen, L., and Lovisolo, M.: Characterization, geometry, temporal evolution and controlling mechanisms of the Jettan Rock-Slide, Northern Norway, in: Engineering Geology for Society and Territory-Volume 2: Landslide Processes, pp. 273–278, Springer, 2015.

Böhme, M., Hermanns, R. L., Oppikofer, T., Fischer, L., Bunkholt, H. S., Eiken, T., Pedrazzini, A., Derron, M.-H., Jaboyedoff, M., Blikra, L. H., et al.: Analyzing complex rock slope deformation at Stampa, western Norway, by integrating geomorphology, kinematics and numerical modeling, Engineering geology, 154, 116–130, 2013.

Böhme, M., Bunkholt, H., Dehls, J., Oppikofer, T., Hermanns, R., Dalsegg, E., Kristensen, L., Lauknes, T. R., and Eriksen, H. Ø.: Geologisk modell og fare-og risikoklassifisering av det ustabile fjellpartiet Gamanjunni 3 i Manndalen, Troms, 2016a.

Böhme, M., Bunkholt, H., Oppikofer, T., Dehls, J., Hermanns, R., Eriksen, H., Lauknes, T., and Eiken, T.: Using 2D InSAR, dGNSS and structural field data to understand the deformation mechanism of the unstable rock slope Gamanjunni 3, northern Norway, in: Landslides and engineered slopes. Experience, theory and practice, pp. 443–449, CRC Press, 2016b.

Böhme, M., Hermanns, R., Gosse, J., Hilger, P., Eiken, T., Lauknes, T., and Dehls, J.: Comparison of monitoring data with paleo–slip rates: cosmogenic nuclide dating detects acceleration of a rockslide, Geology, 47, 339–342, 2019.

https://doi.org/10.5194/egusphere-2026-62
Preprint. Discussion started: 22 January 2026

Bontemps, N., Lacroix, P., Larose, E., Jara, J., and Taipe, E.: Rain and small earthquakes maintain a slow-moving landslide in a persistent critical state, Nature Communications, 11, 780, 2020.

Borgeat, X., Glueer, F., Häusler, M., Hobiger, M., and Fäh, D.: On the variability of the site-response parameters of the active rock slope in Brienz/Brinzauls (Switzerland), Geophysical Journal International, 240, 779–790, 2025.

Braathen, A., Blikra, L. H., Berg, S. S., and Karlsen, F.: Rock-slope failures in Norway; type, geometry, deformation mechanisms and stability., Norwegian Journal of Geology/Norsk Geologisk Forening, 84, 2004.

Brocher, T. M.: Empirical Relations between Elastic Wavespeeds and Density in the Earth's Crust, Bulletin of the Seismological Society of America, 95, 2081–2092, https://doi.org/10.1785/0120050077, 2005a.

Brocher, T. M.: Empirical relations between elastic wavespeeds and density in the Earth's crust, Bulletin of the seismological Society of America, 95, 2081–2092, 2005b.

Cardinali, M., Ardizzone, F., Galli, M., Guzzetti, F., and Reichenbach, P.: Landslides triggered by rapid snow melting: the December 1996–January 1997 event in Central Italy, in: Proceedings 1st Plinius conference on Mediterranean storms, pp. 439–448, Bios Publisher, Cosenza, 2000.

CSG: DMS EW (Version 4.9.21.9.): Centro Sercizi de Geoingegneria (CSG) [Software], https://www.csgsrl.eu/eng/dmsâĂŘsoftware.html, 2007.

Czekirda, J., Etzelmüller, B., Westermann, S., Isaksen, K., and Magnin, F.: Post-Little Ice Age rock wall permafrost evolution in Norway, The Cryosphere, 17, 2725–2754, 2023.

Dai, C., Kilroy, C., Svennevig, K., and Higman, B.: Landslides in Greenland from ArcticDEM time series analysis, Landslides, pp. 1–10, 2025.

Danabasoglu, G., Lamarque, J.-F., Bacmeister, J., Bailey, D., DuVivier, A., Edwards, J., Emmons, L., Fasullo, J., Garcia, R., Gettelman, A., et al.: The community earth system model version 2 (CESM2), Journal of Advances in Modeling Earth Systems, 12, e2019MS001 916, 2020.

Dobry, R., Oweis, I., and Urzua, A.: Simplified procedures for estimating the fundamental period of a soil profile, Bulletin of the Seismological Society of America, 66, 1293–1321, 1976.

Donnini, M., Santangelo, M., Gariano, S. L., Bucci, F., Peruccacci, S., Alvioli, M., Althuwaynee, O., Ardizzone, F., Bianchi, C., Bornaetxea, T., et al.: Landslides triggered by an extraordinary rainfall event in Central Italy on September 15, 2022, Landslides, 20, 2199–2211, 2023.

Eberhardt, E., Stead, D., and Coggan, J.: Numerical analysis of initiation and progressive failure in natural rock slopes—the 1991 Randa rockslide, International Journal of Rock Mechanics and Mining Sciences, 41, 69–87, 2004.

Elvebakk, H.: Borehullslogging med optisk televiewer, Jettan 1, Nordnesfjellet, Kåfjord kommune, Troms, 2013.

Elvebakk, H.: Borehullslogging med optisk televiewer, Bh 2 og Bh 3, Jettan, Nordnesfjellet, Kåfjord kommune, Troms, 2014.

ESRI: ArcGIS Pro (Version 3.1.3.) [Software], https://www.esri.com/enâĂŘus/arcgis/products/arcgisâĂŘpro/overview, 2023.

Etzelmüller, B., Czekirda, J., Magnin, F., Duvillard, P.-A., Ravanel, L., Malet, E., Aspaas, A., Kristensen, L., Skrede, I., Majala, G. D., et al.: Permafrost in monitored unstable rock slopes in Norway–new insights from temperature and surface velocity measurements, geophysical surveying, and ground temperature modelling, Earth Surface Dynamics, 10, 97–129, 2022.

https://doi.org/10.5194/egusphere-2026-62
Preprint. Discussion started: 22 January 2026

Fiddes, J. and Gruber, S.: TopoSCALE v. 1.0: downscaling gridded climate data in complex terrain, Geoscientific Model Development, 7, 387–405, 2014.

Finnegan, N., Brodsky, E., Savage, H., Nereson, A., and Murphy, C.: Seasonal slow landslide displacement is accommodated by mm-scale stick-slip events, Geophysical Research Letters, 49, e2022GL099 548, 2022.

Foglino, V., Foglino, L., Foglino, S., and Lovisolo, M.: New multi-inclinometric geotechnical monitoring systems — the importance of alignment calibration and testing for reliability and correct data interpretation, in: FMGM 2015: Proceedings of the Ninth Symposium on Field Measurements in Geomechanics, edited by Dight, P., pp. 161–171, Australian Centre for Geomechanics, https://doi.org/10.36487/ACG_rep/1508_07_Foglino, 2015.

Frauenfelder, R., Isaksen, K., Lato, M. J., and Noetzli, J.: Ground thermal and geomechanical conditions in a permafrost-affected high-latitude rock avalanche site (Polvartinden, northern Norway), The Cryosphere, 12, 1531–1550, 2018.

Ganerød, G. V.: Geological logging of drill core from borehole NN-01-12 at Jettan, Nordnes mountain in Troms county, Northern Norway, 2013.

Ganerød, G. V.: Geological logging of drill cores from borehole BH 02-13 and BH 03-13 at Jettan, Nordnes mountain in Troms county, Northern Norway, 2014.

Geological Survey of Norway (NGU): Faktaark: Ustabile fjellpartier – Gámanjunni, https://www.nve.no/media/10999/gamanjunni.pdf, accessed October 17, 2025, 2025.

Grämiger, L. M., Moore, J. R., Gischig, V. S., Ivy-Ochs, S., and Loew, S.: Beyond debuttressing: Mechanics of paraglacial rock slope damage during repeat glacial cycles, Journal of Geophysical Research: Earth Surface, 122, 1004–1036, 2017.

Gruber, S. and Haeberli, W.: Permafrost in steep bedrock slopes and its temperature-related destabilization following climate change, Journal of Geophysical Research: Earth Surface, 112, 2007.

Gruber, S., Hoelzle, M., and Haeberli, W.: Permafrost thaw and destabilization of Alpine rock walls in the hot summer of 2003, Geophysical research letters, 31, 2004.

Haakenstad, H. and Breivik, Ø.: NORA3. Part II: precipitation and temperature statistics in complex terrain modeled with a nonhydrostatic model, Journal of Applied Meteorology and Climatology, 61, 1549–1572, 2022.

Haakenstad, H., Breivik, Ø., Furevik, B. R., Reistad, M., Bohlinger, P., and Aarnes, O. J.: NORA3: A nonhydrostatic high-resolution hindcast of the North Sea, the Norwegian Sea, and the Barents Sea, Journal of Applied Meteorology and Climatology, 60, 1443–1464, 2021.

Hadziioannou, C., Larose, E., Coutant, O., Roux, P., and Campillo, M.: Stability of monitoring weak changes in multiply scattering media with ambient noise correlation: Laboratory experiments, The Journal of the Acoustical Society of America, 125, 3688–3695, 2009.

Handwerger, A. L., Rempel, A. W., Skarbek, R. M., Roering, J. J., and Hilley, G. E.: Rate-weakening friction characterizes both slow sliding and catastrophic failure of landslides, Proceedings of the National Academy of Sciences, 113, 10 281–10 286, 2016.

Handwerger, A. L., Lacroix, P., Bell, A. F., Booth, A. M., Huang, M.-H., Mudd, S. M., Bürgmann, R., and Fielding, E. J.: Multi-sensor remote sensing captures geometry and slow-to-fast sliding transition of the 2017 Mud Creek landslide, Scientific Reports, 15, 29 831, 2025.

https://doi.org/10.5194/egusphere-2026-62
Preprint. Discussion started: 22 January 2026

Hauck, Christian and Hilbich, Christin: 4-phase model simulations Gámanjunni, Technical report, Department of Geosciences, University of Freiburg, Albert-Ludwigs-Universität Freiburg, Albertstrasse 23a, 79104 Freiburg, Germany, accessed October 17, 2025, 2018.

Hermanns, R., Oppikofer, T., Anda, E., Blikra, L., Böhme, M., Bunkholt, H., Crosta, G., Dahle, H., Devoli, G., Fischer, L., et al.: Hazard and risk classification for large unstable rock slopes in Norway, Italian Journal of Engineering Geology and Environment, 2013, 245–254, 2013.

Herrmann, R. B.: Computer Programs in Seismology: An Evolving Tool for Instruction and Research, Seismological Research Letters, 84, 1081–1088, https://doi.org/10.1785/0220110096, 2013.

Hilger, P., Hermanns, R. L., Czekirda, J., Myhra, K. S., Gosse, J. C., and Etzelmüller, B.: Permafrost as a first order control on long-term rock-slope deformation in (Sub-) Arctic Norway, Quaternary Science Reviews, 251, 106 718, 2021.

Hobiger, M., Wegler, U., Shiomi, K., and Nakahara, H.: Single-station cross-correlation analysis of ambient seismic noise: application to stations in the surroundings of the 2008 Iwate-Miyagi Nairiku earthquake, Geophysical Journal International, 198, 90–109, 2014.

Høydedata: Høydedata [Dataset], https://hoydedata.no/LaserInnsyn2/, 2024.

Iverson, R. M.: Landslide triggering by rain infiltration, Water resources research, 36, 1897–1910, 2000.

Iverson, R. M.: Regulation of landslide motion by dilatancy and pore pressure feedback, Journal of Geophysical Research: Earth Surface, 110, 2005.

Iverson, R. M. and Major, J. J.: Rainfall, ground-water flow, and seasonal movement at Minor Creek landslide, northwestern California: Physical interpretation of empirical relations, Geological Society of America Bulletin, 99, 579–594, 1987.

Kääb, A. and Røste, J.: Rock glaciers across the United States predominantly accelerate coincident with rise in air temperatures, Nature Communications, 15, 7581, 2024.

Krautblatter, M., Funk, D., and Günzel, F. K.: Why permafrost rocks become unstable: a rock–ice-mechanical model in time and space, Earth Surface Processes and Landforms, 38, 876–887, 2013.

Kristensen, L., Czekirda, J., Penna, I., Etzelmüller, B., Nicolet, P., Pullarello, J. S., Blikra, L. H., Skrede, I., Oldani, S., and Abellan, A.: Movements, failure and climatic control of the Veslemannen rockslide, Western Norway, Landslides, 18, 1963–1980, 2021.

Lacroix, P., Handwerger, A. L., and Bièvre, G.: Life and death of slow-moving landslides, Nature Reviews Earth & Environment, 1, 404–419, 2020.

Lacroix, P., Belart, J. M., Berthier, E., Sæmundsson, Þ., and Jónsdóttir, K.: Mechanisms of landslide destabilization induced by glacier-retreat on Tungnakvíslarjökull area, Iceland, Geophysical Research Letters, 49, e2022GL098 302, 2022.

Larose, E., Carrière, S., Voisin, C., Bottelin, P., Baillet, L., Guéguen, P., Walter, F., Jongmans, D., Guillier, B., Garambois, S., et al.: Environmental seismology: What can we learn on earth surface processes with ambient noise?, Journal of Applied Geophysics, 116, 62–74, 2015.

Le Breton, M., Bontemps, N., Guillemot, A., Baillet, L., and Larose, É.: Landslide monitoring using seismic ambient noise correlation: challenges and applications, Earth-Science Reviews, 216, 103 518, 2021a.

Le Breton, M., Bontemps, N., Guillemot, A., Baillet, L., and Larose, E.: Landslide monitoring using seismic ambient noise correlation: challenges and applications, Earth-Science Reviews, 216, 103 518, https://doi.org/10.1016/j.earscirev.2021.103518, 2021b.

https://doi.org/10.5194/egusphere-2026-62
Preprint. Discussion started: 22 January 2026

Leshchinsky, B., Olsen, M. J., Mohney, C., O'Banion, M., Bunn, M., Allan, J., and McClung, R.: Quantifying the sensitivity of progressive landslide movements to failure geometry, undercutting processes and hydrological changes, Journal of Geophysical Research: Earth Surface, 124, 616–638, 2019.

Liu, Z., Liang, C., Sens-Schönfelder, C., Hu, W., Sun, X., Zhang, T., Xu, R., Jiang, Z., and Jiang, H.: Monitoring crack opening via seismic velocity variation to assess that fatal effect of precipitation for landslide motion, Earth and Planetary Science Letters, 644, 118 922, 2024.

Lussana, C.: seNorge observational gridded dataset. seNorge_2018, versions 21.09 and 21.10. MET report, Report 072021, 2021.

Luu, K.: disba: Numba-accelerated computation of surface wave dispersion, https://pypi.org/project/disba/, accessed: 2025-05-19, 2021.

Magnin, F., Etzelmüller, B., Westermann, S., Isaksen, K., Hilger, P., and Hermanns, R. L.: Permafrost distribution in steep rock slopes in Norway: measurements, statistical modelling and implications for geomorphological processes, Earth Surface Dynamics, 7, 1019–1040, 2019.

Mainsant, G., Larose, E., Brönnimann, C., Jongmans, D., Michoud, C., and Jaboyedoff, M.: Ambient seismic noise monitoring of a clay landslide: Toward failure prediction, Journal of Geophysical Research: Earth Surface, 117, 2012.

Mamot, P., Weber, S., Schröder, T., and Krautblatter, M.: A temperature-and stress-controlled failure criterion for ice-filled permafrost rock joints, The Cryosphere, 12, 3333–3353, 2018.

Moreau, L., Stehly, L., Boué, P., Lu, Y., Larose, E., and Campillo, M.: Improving ambient noise correlation functions with an SVD-based Wiener filter, Geophysical Journal International, 211, 418–426, 2017.

NGU: Faktaark: Ustabile fjellpartier – Jettan, https://geo.ngu.no/api/faktaark/ustabilefjell2/visHovedpunkt.php?more=false&globalid=%7B56DB8DD2-876C-4514-8B0D-A4E825206E85%7D, geological Survey of Norway (NGU). Accessed October 17, 2025, 2025.

Norsar: NORSAR station network, 1971.

NVE: NVEs veileder for sikkerhet mot fjellskred, https://veiledere.nve.no/fjellskred/, accessed October 17, 2025, 2024.

Painter, S. L. and Karra, S.: Constitutive model for unfrozen water content in subfreezing unsaturated soils, Vadose Zone Journal, 13, vzj2013–04, 2014.

Pandas Developers: pandas.DataFrame.resample, https://pandas.pydata.org/docs/reference/api/pandas.DataFrame.resample.html, accessed: 2025-11-17, 2025a.

Pandas Developers: pandas.DataFrame.rolling, https://pandas.pydata.org/docs/reference/api/pandas.DataFrame.rolling.html, accessed: 2025-11-17, 2025b.

Patton, A. I., Rathburn, S. L., and Capps, D. M.: Landslide response to climate change in permafrost regions, Geomorphology, 340, 116–128, 2019.

Patton, A. I., Rathburn, S. L., Capps, D. M., McGrath, D., and Brown, R. A.: Ongoing Landslide Deformation in Thawing Permafrost, Geophysical Research Letters, 48, e2021GL092 959, https://doi.org/https://doi.org/10.1029/2021GL092959, 2021.

Pei, Y., Qiu, H., Zhu, Y., Wang, J., Yang, D., Tang, B., Wang, F., and Cao, M.: Elevation dependence of landslide activity induced by climate change in the eastern Pamirs, Landslides, 20, 1115–1133, 2023.

https://doi.org/10.5194/egusphere-2026-62
Preprint. Discussion started: 22 January 2026

Penna, I., Magnin, F., Nicolet, P., Etzelmüller, B., Hermanns, R., Böhme, M., Kristensen, L., Nöel, F., Bredal, M., and Dehls, J. F.: Permafrost controls the displacement rates of large unstable rock-slopes in subarctic environments, Global and Planetary change, 220, 104 017, 2023a.

Penna, I., Nicolet, P., Hermanns, R., Böhme, M., and Nöel, F.: Preliminary inventory of rock avalanche deposits and their related sources in Norway: Regional distribution, main features and topographic constraints, 2023b.

Perktold, J., Seabold, S., and Taylor, J.: Time Series analysis tsa (Version 0.14.4.) [Software], https://www.statsmodels.org/stable/tsa.html#descriptive-statistics-and-tests, 2023.

Pogrebiskiy, M. and Chernyshev, S.: Determination of the Permeability of the Frozen Fissured Rock Massif in the Vicinity of the Kolyma Hydroelectric Power Station (Oshenka Vodopronishaemosti Merzlogo Greshinovatogo Massiva Gornkh Porod Uchastka Kolmskoy ges), Tech. rep., Corps of Engineers, US Army, Hannover, New Hampshire, 1977.

Quenardel, J.-M. and Zwaan, K. B.: Berggrunnskart MANNDALEN 1633 I, M 1:50000. Foreløpig utgave, preliminary edition, 2008.

Raftery, A. E.: Bayesian model selection in social research, Sociological methodology, pp. 111–163, 1995.

Rantanen, M., Karpechko, A. Y., Lipponen, A., Nordling, K., Hyvärinen, O., Ruosteenoja, K., Vihma, T., and Laaksonen, A.: The Arctic has warmed nearly four times faster than the globe since 1979, Communications earth & environment, 3, 168, 2022.

Ravanel, L., Magnin, F., and Deline, P.: Impacts of the 2003 and 2015 summer heatwaves on permafrost-affected rock-walls in the Mont Blanc massif, Science of the Total Environment, 609, 132–143, 2017.

Rechberger, C., Fey, C., and Zangerl, C.: Structural characterisation, internal deformation, and kinematics of an active deep-seated rock slide in a valley glacier retreat area, Engineering Geology, 286, 106 048, 2021.

Rønning, J., Dalsegg, E., Heincke, B., Juliussen, H., and Tønnesen, J.: Geofysiske målinger på Nordnesfjellet sommeren 2007, Kåfjord kommune, Troms, NGU Rapport 2008.024, 2008.

Ruggeri, P., Fruzzetti, V. M., Ferretti, A., and Scarpelli, G.: Seismic and rainfall induced displacements of an existing landslide: Findings from the continuous monitoring, Geosciences, 10, 90, 2020.

Saemundsson, T., Petursson, H., Kneisel, C., and Beylich, A.: Monitoring of the Tjarnardalir landslide, in central North Iceland, in: First North America Landslide Conference, Schaefer VR, Schuster RL, Turner AK (eds). AEG Publication, vol. 23, pp. 1029–1040, 2007.

scikit-learn developers: MinMaxScaler (Version 0.24.) [Software], https://scikit-learn.org/stable/modules/generated/sklearn.preprocessing.MinMaxScaler.html, 2024.

SciPy Developers: scipy.signal.savgol_filter, https://docs.scipy.org/doc/scipy/reference/generated/scipy.signal.savgol_filter.html, accessed: 2024-11-17, 2025.

seNorge: Varsom seNorge [Dataset], https://www.senorge.no/, 2024.

Sens-Schönfelder, C. and Wegler, U.: Passive image interferometry and seasonal variations of seismic velocities at Merapi Volcano, Indonesia, in: Seismic Interferometry: History and Present Status, Society of Exploration Geophysicists, ISBN 9781560801504, https://doi.org/10.1190/1.9781560801924, 2008.

Shugar, D. H., Jacquemart, M., Shean, D., Bhushan, S., Upadhyay, K., Sattar, A., Schwanghart, W., McBride, S., De Vries, M. V. W., Mergili, M., et al.: A massive rock and ice avalanche caused the 2021 disaster at Chamoli, Indian Himalaya, Science, 373, 300–306, 2021.

https://doi.org/10.5194/egusphere-2026-62
Preprint. Discussion started: 22 January 2026

Skrede, I.: Jettan, Nordnesfjellet, Kåfjord, Troms–indre geometri og struktur, kinematikk og styrande faktorar av eit ustabilt fjellparti, basert på strukturellanalyse, geomorfologi og overvakingsdata, Master's thesis, UiT Norges arktiske universitet, 2013.

Svennevig, K., Hicks, S. P., Forbriger, T., Lecocq, T., Widmer-Schnidrig, R., Mangeney, A., Hibert, C., Korsgaard, N. J., Lucas, A., Satriano, C., et al.: A rockslide-generated tsunami in a Greenland fjord rang Earth for 9 days, Science, 385, 1196–1205, 2024.

Themeßl, M. J., Gobiet, A., and Heinrich, G.: Empirical-statistical downscaling and error correction of regional climate models and its impact on the climate change signal, Climatic Change, 112, 449–468, 2012.

Vick, L. M., Berg, J. N., Eggers, M., Hormes, A., Skrede, I., and Blikra, L. H.: Keynote Lecture: The Jettan Rockslide—An Engineering Geological Overview, Understanding and Reducing Landslide Disaster Risk: Volume 6 Specific Topics in Landslide Science and Applications 5th, pp. 289–315, 2021.

Vionnet, V., Brun, E., Morin, S., Boone, A., Faroux, S., Le Moigne, P., Martin, E., and Willemet, J.-M.: The detailed snowpack scheme Crocus and its implementation in SURFEX v7. 2, Geoscientific model development, 5, 773–791, 2012.

Walden, J., Jacquemart, M., Higman, B., Hugonnet, R., Manconi, A., and Farinotti, D.: Landslide activation during deglaciation in a fjord-dominated landscape: observations from southern Alaska (1984–2022), Natural Hazards and Earth System Sciences, 25, 2045–2073, 2025.

Wathelet, M., Chatelain, J.-L., Cornou, C., Di Giulio, G., Guillier, B., Ohrnberger, M., and Savvaidis, A.: Geopsy: A User-Friendly Open-Source Tool Set for Ambient Vibration Processing, Seismological Research Letters, 91, 1878–1889, https://doi.org/10.1785/0220190360, 2020.

Westermann, S., Ingeman-Nielsen, T., Scheer, J., Aalstad, K., Aga, J., Chaudhary, N., Etzelmüller, B., Filhol, S., Kääb, A., Renette, C., Schmidt, L. S., Schuler, T. V., Zweigel, R. B., Martin, L., Morard, S., Ben-Asher, M., Angelopoulos, M., Boike, J., Groenke, B., Miesner, F., Nitzbon, J., Overduin, P., Stuenzi, S. M., and Langer, M.: The CryoGrid community model (version 1.0) – a multi-physics toolbox for climate-driven simulations in the terrestrial cryosphere, Geoscientific Model Development, 16, 2607–2647, https://doi.org/10.5194/gmd-16-2607-2023, 2023.

Zwaan, K. B., Dangla, P., and Quenardel, J.-M.: Berggrunnskart Kåfjord 16342, 1:50 000, forløpig utgave, 2006.